Monthly Notices
of the
ROYAL ASTRONOMICAL SOCIETY

MNRAS **468,** 4056–4076 (2017)
Advance Access publication 2017 March 22

doi:10.1093/mnras/stx699

The features of the Cosmic Web unveiled by the flip-flop field

Sergei F. Shandarin* and Mikhail V. Medvedev

Physics and Astronomy, University of Kansas, 1251 Wescoe Hall Drive, Malott Hall, #1082, Lawrence, KS 66045, USA

Accepted 2017 March 20. Received 2017 March 17; in original form 2016 September 27

ABSTRACT

Currently the dark matter environment is widely accepted as a framework for understanding of the observed structure in the universe. *N*-body simulations are indispensable for the analysis of the formation and evolution of the dark matter web. Two primary fields – density and velocity fields – are used in most of studies. Dark matter provides two additional fields that are unique for collisionless media only. They are the multistream field in Eulerian space and flip-flop field in Lagrangian space. The flip-flop field represents the number of sign reversals of an elementary volume of each collisionless fluid element. This field can be estimated by counting the sign reversals of the Jacobian at each particle at every time step of the simulation. The Jacobian is evaluated by numerical differentiation of the Lagrangian submanifold, i.e. the three-dimensional dark matter sheet in the six-dimensional space formed by three Lagrangian and three Eulerian coordinates. We present the results of the statistical study of the evolution of the flip-flop field from $z = 50$ to the present time $z = 0$. A number of statistical characteristics show that the pattern of the flip-flop field remains remarkably stable from $z \approx 30$ to the present time. As a result the flip-flop field evaluated at $z = 0$ stores a wealth of information about the dynamical history of the dark matter web. In particular one of the most intriguing properties of the flip-flop is a unique capability to preserve the information about the merging history of haloes.

Key words: methods: numerical – dark matter – large-scale structure of Universe – cosmology: theory.

1 INTRODUCTION

Modern redshift surveys such as 2dF Galaxy Redshift Survey[1] and the Sloan Digital Sky Survey[2] as well as others reveal the wealth of structures in the spatial distribution of galaxies. A useful abstraction helping to comprehend the complexity of the structure has been provided by the skeleton of the web introduced by the adhesion approximation (Gurbatov, Saichev & Shandarin 1985, 1989, 2012; Hidding et al. 2012a,b). Its geometrical version designs a tiling of three-dimensional space by irregular three-dimensional tiles associated with voids. The surfaces of the tiles are associated with walls/pancakes, the edges – with filaments and the vertices – with the haloes. The geometrical model obviously highly simplifies the Cosmic Web especially its interior structure since it does not trace the details in the complex distribution of mass inside the walls, filaments and haloes. However the skeleton looks qualitatively quite realistic revealing the multiscale nature of the web. For instance, it indicated for the first time the presence of substructures in voids (Kofman et al. 1992).

Historically, haloes have attracted the most of attention in theoretical studies of the large-scale structure formation. From the observational point of view, haloes are most closely related to galaxies, galaxy groups and clusters of galaxies, which provide the bulk of information about the structures in the Universe. However, direct modelling of galaxy formation based on fundamental laws of physics is precluded by enormous complexity of the physical processes involved. In addition to the gravitational coupling with dark matter (hereafter DM) structure baryons participate in extremely complex hydrodynamical and thermal processes including star formation and the stellar wind feedback, shocks and supernovae explosions, gas accretion on to black holes in active galactic nuclei and the feedback via relativistic jets to name just some.

Hence various semi-analytic models of galaxy formation have been suggested, see e.g. Benson (2012) and references therein. In particular, it has been argued that galaxies are formed in the host DM haloes of corresponding masses. The DM haloes themselves are formed in a chain of mergers of smaller DM haloes which may start from tiny haloes of planet masses (Diemand, Moore & Stadel 2005). When two or more haloes merge, their remnants may survive for a long time as subhaloes and/or streams within the resultant halo. Therefore, DM haloes are likely to have a nesting structure where each subhalo may include a number of even smaller subhaloes down to the smallest haloes allowed by the initial power spectrum (Ghigna et al. 1998; Diemand et al. 2005).

* E-mail: sergei@ku.edu
[1] http://msowww.anu.edu.au/2dFGRS/
[2] http://www.sdss.org/

Dark matter structure results from the gravitational growth of the initial Gaussian perturbations of density. It is shaped by the non-linear collisionless gravitational dynamics. Being very complex, it is still considerably simpler than baryonic physics assuming that the hydrodynamical and thermal processes in baryons include star formation and other complex physical processes mentioned before. Therefore, it is more feasible to build the model of the DM web based on fundamental physical laws with invoking heuristic assumptions. Cosmological *N*-body simulations play indispensable role in the studies of the DM web providing the most reliable data on the evolution of the web in highly non-linear regime. However identifying the basic elements of the web (i.e. haloes, filaments, walls and voids) represents a difficult problem even in pure DM *N*-body simulations where all dynamical information is readily available, see e.g. Colberg et al. (2008), Knebe et al. (2013) and Cautun et al. (2014).

In early cosmological *N*-body simulations, the haloes were loosely defined as compact concentrations of the simulation particles in configuration space. A particularly popular simple technique used for this purpose and called the friends of friends (FOF) algorithm was adopted from percolation analysis (Zeldovich, Einasto & Shandarin 1982; Shandarin 1983; Davis et al. 1985). According to this method, one first finds all 'friends' of each particle by linking every particle in the simulation with all neighbours separated by less than a chosen distance – the linking length. Then applying the criterion: a friend of my friend is my friend, one can identify all groups of particles consisting of friends at a given linking length. Choosing a particular value of the linking length [often ∼20 per cent of the mean particle separation, Davis et al. (1985)] one can select a particular set of groups and call them haloes. A number of improved versions of FOF have been developed: Couchman & Carlberg (1992); Suginohara & Suto (1992); van Kampen (1995); Summers, Davis & Evrard (1995); Klypin et al. (1999); Okamoto & Habe (1999) just to mention a few. More, Diemer & Kravtsov (2015) conducted a thorough study of overdensities and masses of FOF haloes. In particular, they concluded that the boundaries of FOF haloes do not correspond to a single density threshold but to a range of densities and the average overdensity depends on the density profile (concentration) of haloes contrary to a popular belief that it is ∼180. They argued that the splashback radius corresponding to the location of the outermost density caustic in the spherical models of secondary collapse is 'the most natural definition of a physical halo boundary'. We would like to emphasize that the mentioned above caustic is also the location in Eulerian space of the particles experienced the first flip-flop. Others more sophisticated methods that identify both haloes and subhaloes have been suggested as well, for review see Knebe et al. (2013) and references therein. Some of them rely only on the particle positions, others use also the phase-space information. The methods using only the configuration space information regardless of their sophistication may suffer from projection effect that causes dynamically distinct structures in phase space temporally to overlap in configuration space and thus to be indistinguishable. We illustrate this by a simple one-dimensional example that also illustrates the flip-flop field and Lagrangian submanifold that are the major focus of this paper.

1.1 One-dimensional example

Let us consider a halo simulated in one-dimensional case from random but smooth initial condition. The figure provides four representations of the halo: (i) in phase space $v(x)$ (top left), (ii) as the density field in the halo $\log(\rho(x))$ (bottom left), (iii) as the flip-flop field corresponding to the halo $n_{\rm ff}(q)$ (bottom right) and (iv) as the Lagrangian submanifold of the halo (middle left and top right). A flip-flop event in one-dimensional space is simply a swap of the order of two neighbouring particles: for instance $x(q_{i+1}, t) > x(q_i, t)$ but at the next time step $x(q_{i+1}, t + \delta t) < x(q_i, t + \delta t)$ or vice versa. Thus the flip-flop field is the number of flip-flops experienced by every particle as a function of Lagrangian coordinate q. The Lagrangian submanifold is displayed twice as $q(x)$ on the left and as $x(q)$ on the right. This allows a more convenient comparison with other plots in the same column. Colours mark different peaks identified in Lagrangian space as the segments between two minima of the flip-flop field. Since the flip-flop field is an integral field, both maxima and minima can be reached in more than one point although in practice this happens more often in minima. Such minima are shown as dashed lines in phase space and in both plots of Lagrangian submanifold.

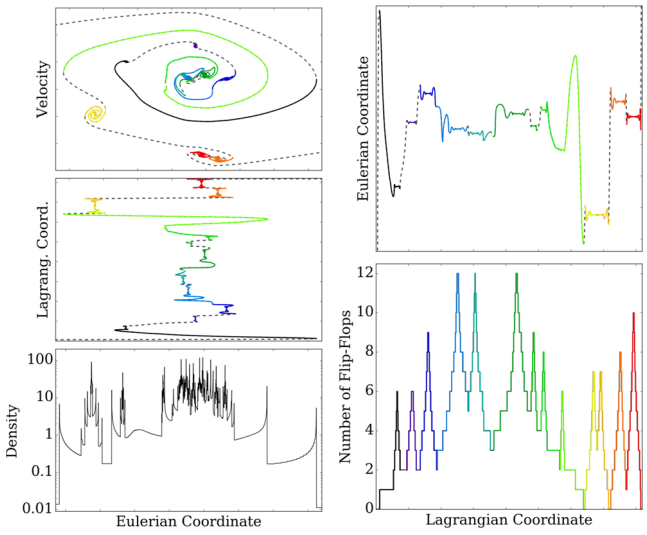

Figure 1. Illustration of a one-dimensional halo simulated from random but smooth initial condition. The panels are arranged as follows: phase space $v(x)$ (top left), density distribution $\log(\rho(x))$ (bottom left), the flip-flop field $n_{\rm ff}(q)$ (bottom right) and Lagrangian submanifold $x(q)$ (on the right) and $q(x)$ (on the left). Different colours in all colourful panels show particles in different subhaloes. All plots are made at the same instant.

The figure displays a complicated substructure consisting of a number of subhaloes and streams marked by different colours in phase space. Restricting the analysis by using only the coordinates of particles means that the complicated phase-space curve must be projected on the horizontal. It is obvious from the figure that distinguishing some individual subhaloes in configuration space is impossible even in a one-dimensional case. For instance, the pair of subhaloes in red at the bottom of the phase-space panel is currently projected on the central part of the halo and thus cannot be identified as separate subhaloes in the density field as the bottom panel shows. But at a later time it approximately will take place of the yellow subhalo on the left and thus may be identified as a separate pair of subhaloes. It becomes even more challenging in three-dimensional case, see e.g. Knebe et al. (2013), Hoffmann et al. (2014) and reference therein.

From Fig. 1 one can also see that a halo as well as subhaloes can be naturally defined as the regions in Eulerian space where the number of streams is greater than one (Shandarin, Habib & Heitmann 2012; More et al. 2015; Ramachandra & Shandarin 2015,

2017). However, this approach also is not free of the contamination effects due to projection effects. Using all dynamical information available in phase space helps in solving this problem; however, this is complicated by the fact that phase space is not a metric space, see e.g. Ascasibar & Binney (2005). Evaluating distances in phase space requires additional parameter with the dimensions of time. Unfortunately, the time parameter is not universal for the whole halo. For illustration, consider again a simple example shown in Fig. 1. The spiraling time of two red subhaloes shown on the bottom of the figure is mostly determined by the density due to the subhaloes themselves $\tau_{\rm sh} \propto \rho_{\rm sh}^{-1/2}$ rather than by the total density dominated by the central part of the halo. This is because they spend a relatively short time in the spatial vicinity of the centre. They live outside the central region of the halo the most of time since they move with lower speed there. In the outskirts of the main halo, their dynamical time is determined primarily by their own densities. Thus finding the relevant local time requires identification of a subhalo in phase space which in turn requires the knowledge of the characteristic time of the same subhalo for making the corresponding patch of phase-space metric. One way overcoming this circular reasoning problem was suggested by Ascasibar & Binney (2005). The method dubbed FiEstAS estimates the underlying density field from a discrete set of sample points without a metric. It assigns a volume to each point by means of a binary tree and then computes density by integrating over an adaptive kernal. It might be also possible to develop some iterative technique but we have tried a new completely different approach.

In order to outline the main idea of this new method, we begin with a closer examination of the one-dimensional example introduced above. Let us follow along the phase-space curve in the top left panel of Fig. 1 starting from the top point of the spiral on the left boundary of the box through the bottom point on the right boundary of the box. Along this path, the initial (Lagrangian) coordinates $q_{\rm i}$ of the particles, which are in essence their IDs and thus are immutable, increase monotonically while their final (Eulerian) coordinates $x_{\rm i}$ are not monotonic. This is also seen in the top right panel of Fig. 1 showing the Lagrangian submanifold of the halo which is the curve $x = x(q; t)$. The analogue of this phenomenon in a multidimensional space is a formal change of the sign of the volume of a fluid element when it turns inside out. The volume of a fluid element is a continuous function of time; therefore, between the states of the volume with different signs it must be zero. At this moment in three-dimensional space, it collapses into a piece of a two-dimensional surface called a caustic and its density becomes infinite. The caustic concept is of cause a mathematical abstraction useful only when the discreteness effects can be neglected.

The total number of flip-flops experienced by every fluid element by the time corresponding to the top left panel is shown in the bottom right panel of Fig. 1. We will refer to it as a flip-flop field. Colours show individual peaks of the flip-flop field in Lagrangian coordinates. The correspondence of the flip-flop peaks in Lagrangian space to the individual subhaloes in the phase space is remarkable. Note that the tidal streams and haloes are also easily, unambiguously and robustly identified via the flip-flop field, cf. the bottom right and top left panels of Fig. 1. Using the flip-flop field in Lagrangian space is the key idea of a new approach to the analysis of DM haloes.

Zel'dovich (1970) was the first who mentioned the flip-flop phenomena in cosmological context. Later on it was used by Arnold, Shandarin & Zeldovich (1982) in the study of generic caustics and also discussed in the review by Shandarin & Zeldovich (1989). Recently, the flip-flop phenomenon was used in the studies of a few specific problems (Shandarin & Medvedev 2014, 2016). Vogelsberger & White (2011) (see also references therein) invoked it for the study of 'the properties of fine-grained phase-space streams and their associated caustics' by 'integrating the geodesic deviation equation' in cosmological *N*-body simulations. Although the counts of caustics were used for computing some one-point statistics, the concept of a field in Lagrangian space was not even mentioned.

Another method called ORIGAMI was suggested in Falck et al. (2012) and Neyrinck et al. (2015). This detects folds in the Lagrangian-to-Eulerian mapping, categorizing each particle (as void, wall, filament or halo) according to the number of orthogonal axes along which folds occur. Neyrinck (2012) also looked at the connectivity of streams in Lagrangian space. In this approach, a binary field with two values +1 and −1 corresponding to positive and negative parities of local Lagrangian volumes was introduced. The values of our flip-flop field can be any non-negative integer and its peaks play the key role in our study.

From dynamical point of view, a subhalo can be described as a set of particles participating in oscillatory motions about some centre (centre of the subhalo) which in turn orbits about the centre of the halo. The both amplitudes of the oscillations of a subhalo in configuration and velocity spaces are significantly smaller than the corresponding sizes of the halo. The characteristic times of the oscillations are also significantly shorter than the corresponding time of the orbiting of the subhalo around the centre of the halo see e.g. (Vogelsberger & White 2011, p. 1424). A similar reason explains why the orbits of planet's satellites have shorter periods than the period of the planet orbiting the Sun.

In a simple one-dimensional halo without subhaloes, the number of flip-flops becomes a counter of full orbits: two flip-flops per a full orbit. It is worth mentioning that in such a halo the periods of orbits become shorter as the particle gets closer to the centre because the mean density within smaller orbits is higher than that within the larger orbits since the period is proportional to $\tau \propto <\rho>^{-1/2}$. The major goal of this paper is to investigate the properties of the flip-flop field and three-dimensional *N*-body simulation and explore its potential usefulness for identifying the DM web, i.e. haloes, filaments, walls/pancakes, voids and their substructures.

1.2 Flip-flop field in two dimensions

Now we consider a two-dimensional example that may help to bridge the visualization gap between one- and three-dimensional.

The two-dimensional example is based on a simple *N*-body simulation in the EdS cosmological model with 2048^2 particles with equivalent mesh for computing CIC density and gravitational force via Fast Fourier Transform. The initial power spectrum was $P \propto k^{-1}$ that corresponds to $P \propto k^{-2}$ in 3D in some important statistical aspects. The initial amplitude was normalized to give linear $\delta_{\rm rms} = 1$ at the scalefactor $a = 1$. The purpose of the simulation was to produce a single halo and evolve it for a long time in order to see how the structure originates and evolves in the flip-flop field. In particular, how fast it gets erased or smeared by non-linear processes or/and numerical noise.

Fig. 2 shows four stage in the evolution at $a \approx 1.0, 2.3, 3.4$ and 58.7. Four panels on the left show the CIC density in Eulerian space and the panels on the right show the corresponding flip-flop fields in Lagrangian space. Although the colours look similar in all plots, they have very different meanings. The density plots use the logarithmic scale with the range in each plot $-1 \le \log_{10}\rho \le max(\log_{10}\rho)$. The flip-flop plots use linear scales with ranges $0 \le n_{\rm ff} \le \max(n_{\rm ff})$. The pattern in the flip-flop field evolves quite

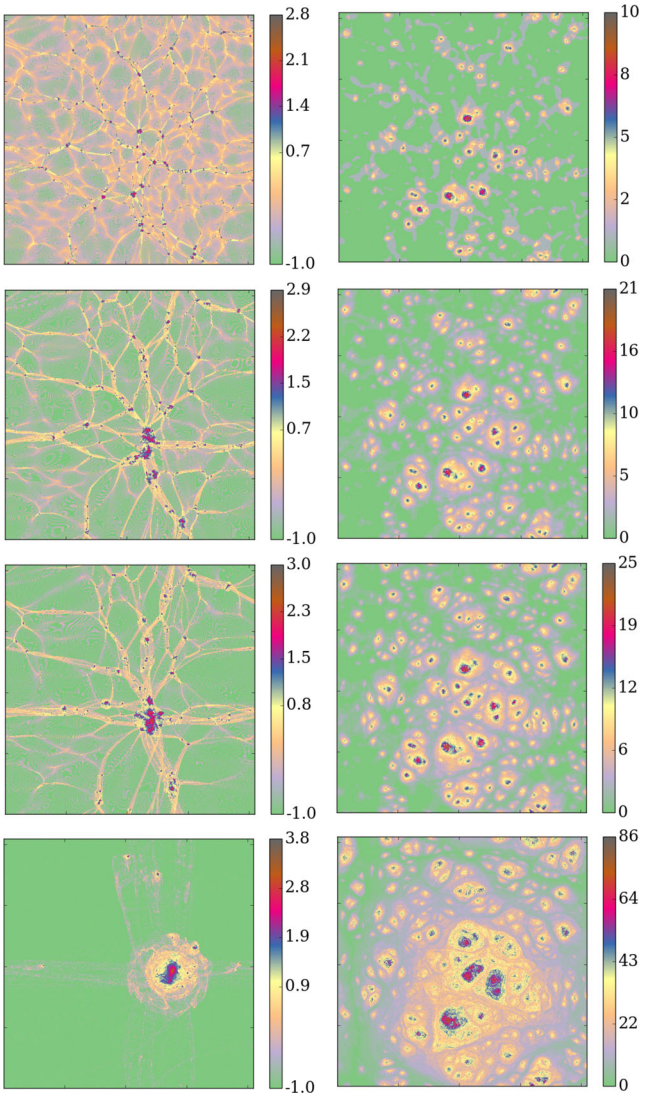

Figure 2. Evolution of structure in two-dimensional *N*-body simulation. Four stages are shown at $a \approx 1.0, 2.3, 3.4$ and 58.7 from top to bottom. The density perturbation linearly extrapolated would result in $\delta_{\rm rms} = 1$ at $a = 1$. The CIC density fields in Eulerian space are shown in the left-hand column. The corresponding flip-flop fields in Lagrangian space are shown on the right. The colour bars show $\log_{10}(\rho/\bar{\rho})$ and $n_{\rm ff}$ in the left-hand and right-hand columns respectively.

rapidly at the beginning of the non-linear stage. It needless to say that before shell crossing the field did not exist or was equal to zero at every point if one feels that it is more preferable definition. However, at the scalefactors approximately between 3 and 4 the geometry of the landscape of the flip-flop almost freezes. The field continues to grow as the increasing range of the colour legends shows but the geometrical pattern evolves very little. For instance, all major peaks seen in the bottom panel corresponding to $a \approx 58.7$ could be easily identified in two middle panels corresponding to $a \approx 2.3$ and 3.4. It is worth stressing that the most of haloes approximately corresponding to individual compact red peaks in the density plots have not completed merging into the final halo yet. However practically all isolated peaks in the right-hand column are merged in the left-hand column at $a = 58.7$ shown at the bottom panels. The areas of the regions shown in green in the flip-flop field may serve as visual indicator of the mass outside of the web. Here we do not show the results of the quantitative statistical analysis as they are similar to that in three-dimensional case presented in the following sections.

The paper is organized as follows. Section 2 explains the method in three dimensions in detail and Section 3 describes the *N*-body simulation used in the study of the flip-flop field properties. After having presented the methodology in the previous sections, we provide three-dimensional illustrations in Section 4. Then we discuss a number of statistical properties of the flip-flop field and in particular its peaks in Section 5. We also compare some properties of the flip-flop field with that of density and gravitational potential fields in Lagrangian space. In Section 6, we show that each Amiga Halo Finder (AHF) halo contains a maxim of flip-flop fields. We present the results of the study of substructure evolution in the largest halo of the simulation in Section 7. Section 8 is a short summary of the results and conclusions.

2 METHOD

We propose a novel approach to the exploration of the DM web in cosmological *N*-body simulations. So far most of the studies used either the particles, or density field in Eulerian space, or the velocity of the particles or gravitational potential field or various combinations of the above quantities. We will use the field in Lagrangian space formed by the number of turns inside out experienced by each DM fluid particle which we call a flip-flop field $n_{\rm ff}(\boldsymbol{q}; a(t))$. We estimate the number of flip-flops experienced by each *N*-body particle by analysing the mapping $\boldsymbol{x} = \boldsymbol{x}(\boldsymbol{q}; a(t))$ at chosen times characterized by the value of the scalefactor $a(t)$ normalized to the present epoch $a(z = 0) = 1$. The particle coordinates $\boldsymbol{x}$ and $\boldsymbol{q}$ are in Eulerian and Lagrangian spaces respectively. The Lagrangian coordinates are the comoving positions of the particles on a regular grid corresponding to the unperturbed initial state. Assuming DM to be cold this mapping, referred to as a Lagrangian submanifold, is a three-dimensional sheet in the six-dimensional space $(\boldsymbol{q}, \boldsymbol{x})$.

The method based on a concept of a DM sheet $\boldsymbol{v} = \boldsymbol{v}(\boldsymbol{x}; t)$ in phase space was successfully employed to improve accuracy of the estimates of the density, velocity and other parameters in standard cosmological *N*-body simulations (Abel, Hahn & Kaehler 2012; Shandarin et al. 2012). The major difference between this concept and the conventional one lies in a different interpretation of the role of the particles in the simulations. Namely, how they represent the state and evolution of the continuous DM medium. In contrast to the common interpretation of particles as carriers of mass, the new approach treats them as massless tracers of the cold DM flows. Geometrically they represent the vertices of a tessellation of the three-dimensional DM sheet in six-dimensional phase space. As a simplest approximation, the mass may be assumed to be uniformly distributed inside each tetrahedron of the tessellation (Abel et al. 2012; Shandarin et al. 2012; Hahn, Abel & Kaehler 2013). However, the density field within the tetrahedra can be approximated to linear or higher order and the tessellation can be adaptively refined which results in further considerable improvement of the estimates of density, velocity and other fields in the regions of strong non-linearity (Powell & Abel 2015; Hahn & Angulo 2016; Sousbie & Colombi 2016).

The particles being the vertices of the tessellation tetrahedra carry all information available in *N*-body simulations about the evolution of the cold DM fluid. It is worth stressing that the 3D phase-space sheet remains continuous in both six-dimensional phase $(\boldsymbol{x}, \boldsymbol{v})$ and $(\boldsymbol{q}, \boldsymbol{x})$ spaces due to the Liouville theorem. In particular, the variations of tetrahedra sizes and volumes result in the corresponding

change of the tetrahedra densities. This property is especially valuable because it makes the tessellation self-adaptive to the growth of density perturbations with time.

The DM phase-space sheet cannot cross itself in the case of a continuous medium which is an excellent model for cold DM down to scales of the order of a characteristic DM particle separation. However, the most of N-body simulations use particles that are more massive than physical DM particles by many orders of magnitude. Thus on scales smaller than the mass resolution scale, the simulations are strongly affected by the discreteness effects that are fiercest at the centres of DM haloes. One of these effects is self-crossing of the DM phase-space sheet. However, the Lagrangian submanifold $\boldsymbol{x} = \boldsymbol{x}(\boldsymbol{q}; a(t))$ in six-dimensional space never crosses itself.

Although both $(\boldsymbol{x}, \boldsymbol{v})$ – and $(\boldsymbol{q}, \boldsymbol{x})$ – spaces contain all the information about a dynamical system allowing to compute the whole evolution from $\boldsymbol{q}$ to $\boldsymbol{x}$ as well as from $\boldsymbol{x}$ to $\boldsymbol{q}$ (see e.g. Landau & Lifshitz 2008) they obviously have very different properties. For instance, an advantage of the former consists in ability to calculate the kinetic energy of the system while an advantage of the latter consists in being a *metric* space. Therefore, the latter is superior to the former in the analysis of geometry of the structure. Moreover, the Lagrangian submanifold $\boldsymbol{x} = \boldsymbol{x}(\boldsymbol{q})$, is a single-valued function, unlike the phase-space sheet $\boldsymbol{v} = \boldsymbol{v}(\boldsymbol{x})$ and $\boldsymbol{x} = \boldsymbol{x}(\boldsymbol{v})$ which are multivalued in a projection on arbitrary three-dimensional space formed by any three axes out of six available $(\boldsymbol{x}, \boldsymbol{v})$ in the non-linear regime after shell crossing.

One way of identifying flip-flops is to follow the changes of sign of the tetrahedra's volumes in the tessellation of the dark matter sheet but we estimate the Jacobian directly on particles without invoking the tetrahedra. Identifying flip-flop events in three dimensions can be done by numerical computing the partial derivatives $\partial x_i/\partial q_j$ on particles and then estimating the Jacobian $J(\boldsymbol{q}, t) = \det(\partial x_i/\partial q_j)$ on each particle at each time step.[3] If the sign of the Jacobian changes, the number of flip-flops for the corresponding particles is increased by one. We show that the flip-flop field $n_{\rm ff}(\mathbf{q}; a)$ at fixed a exhibits features in generic three-dimensional N-body simulation similar to those described in one- and two-dimensional simulations. The flip-flop field was computed in a modified version of a publicly available cosmological TreePM/SPH code GADGET (Springel 2005).

3 N-BODY SIMULATIONS

The initial conditions were generated with NGenIC code[4] with the standard Λ cold dark matter (ΛCDM) cosmology, $\Omega_m = 0.3$, $\Omega_\Lambda = 0.7$, $\Omega_b = 0$, $\sigma_8 = 0.9$, $h = 0.7$ and the initial redshift $z = 50$. A set of simulations were carried out with a box $1\,h^{-1}$ Mpc and total mass $M_{\rm b,dm} \approx 1.2 \times 10^{11}\,{\rm M}_\odot$. For illustration purposes, we present two simulations with 128^3, $m_{\rm part} \approx 5.7 \times 10^4\,{\rm M}_\odot$ and 256^3, $m_{\rm part} \approx 7.1 \times 10^3\,{\rm M}_\odot$ DM particles with the force resolution of $1.5\,h^{-1}$ and $0.75\,h^{-1}$ kpc respectively. The chosen size of the box is obviously too small for the purpose of deriving statistically valid properties of the haloes. However the main purpose of this work is different, namely we would like to demonstrate that the flip-flop field of haloes in a highly non-linear dynamic state retains rich information about the haloes and their substructures as well as about their merging histories. We mark the epochs by the values of the scalefactor a with $a = 1$ corresponding to the present time with $z = 0$. It is worth mentioning that the common parts of the initial Fourier spaces in two simulations have been generated with the same random numbers. Therefore, the meaningful structures in the low-resolution simulation should also exist in the higher resolution simulation.

It is always useful to have a visual concept of any structure when its geometry or/and topology is discussed. The visualization of the major object of our analysis – the submanifold $\boldsymbol{x} = \boldsymbol{x}(\boldsymbol{q}; a(t))$ – is obviously out of question not only in three dimensions with $2N = 6$ but even in two dimensions with $2N = 4$. Its projection on $\boldsymbol{x}$ – space is familiar in the form of ubiquitous dot plots illustrating the results of various N-body simulations. We are interested in visual illustration of the projections on $\boldsymbol{q}$ – space that encounters additional problems compared to the visualization of $\boldsymbol{x}$ – space outlined below.

4 VISUALIZATION OF FLIP-FLOP FIELD IN THREE DIMENSIONS

4.1 Entire simulation box

The top part of Fig. 3 shows the map of the excursion set $n_{\rm ff}(\boldsymbol{q}, z = 0) \geq 6$ in the entire simulation box to Eulerian space. The sizes and colours (from blue to red) of the particles represent the number of flip-flops. Boosting the sizes of less abundant particles with high flip-flop numbers allows to see them in crowded regions dominated by numerous particles with low flip-flop values.

Illustrating the flip-flop field in Lagrangian 3D space represents even more difficult problem than the Cosmic Web in Eulerian space. This is because the dense regions of the web occupy a smaller fraction of the volume in $\boldsymbol{x}$ – space as can be seen in the top of Fig. 3. But the fraction of the volume with $n_{\rm ff} \geq 6$ occupies considerably greater volume in $\boldsymbol{q}$ – space as the bottom of Fig. 3 demonstrates. It shows the dot plot of the corresponding flip-flop field in $\boldsymbol{q}$ – space with the same colour coding. One can see that the flip-flop field has a large number of distinct peaks occupying the most of Lagrangian space however it is not as detailed as in two-dimensional case (Fig. 2) because some of the distant peaks are hidden beneath the nearby structures in the projection on two-dimensional plane.

In order to reveal much greater richness and complexity of the structure of subhaloes in the flip-flop field, we also plot a set of two-dimensional slices through Lagrangian box in Fig. 4. The figure shows eight XZ slices equally spaced along y-axis through the entire 256^3 simulation box. The sequence of slices is ordered from the top left to bottom right panels. In order to suppress numerical noise, we smoothed $n_{\rm ff}$ field with Gaussian filter with the size being equal to the separation of particles in Lagrangian space. The colours are explained in the caption. A complex hierarchy of $n_{\rm ff}$ peaks is revealed in considerably greater detail however at the cost of losing a three-dimensional perspective. Unfortunately, this is a typical trade of one for the other.

Fig. 5 illustrates the effects of low pass filtering of the flip-flop field. It displays four panels of a two-dimensional slice through the highest peak ($n_{\rm ff} = 616$) of the flip-flop field at $z = 0$. The top left panel shows the raw field and the top right, bottom left and bottom right panels show the filtered fields with Gaussian window of size 0.5, 1.0 and 1.5 in the units of the particle separation in Lagrangian space. Filtering was done in 3D space. The major effect of filtering is

[3] The derivatives $\partial x_i/\partial q_j$ (where x_i and q_j are respectively Eulerian and Lagrangian coordinates of particles) were computed by using low-noise Lanczos differentiators, see http://www.holoborodko.com/pavel/numerical-methods/numerical-derivative/lanczos-low-noise-differentiators/

[4] See h-its.org

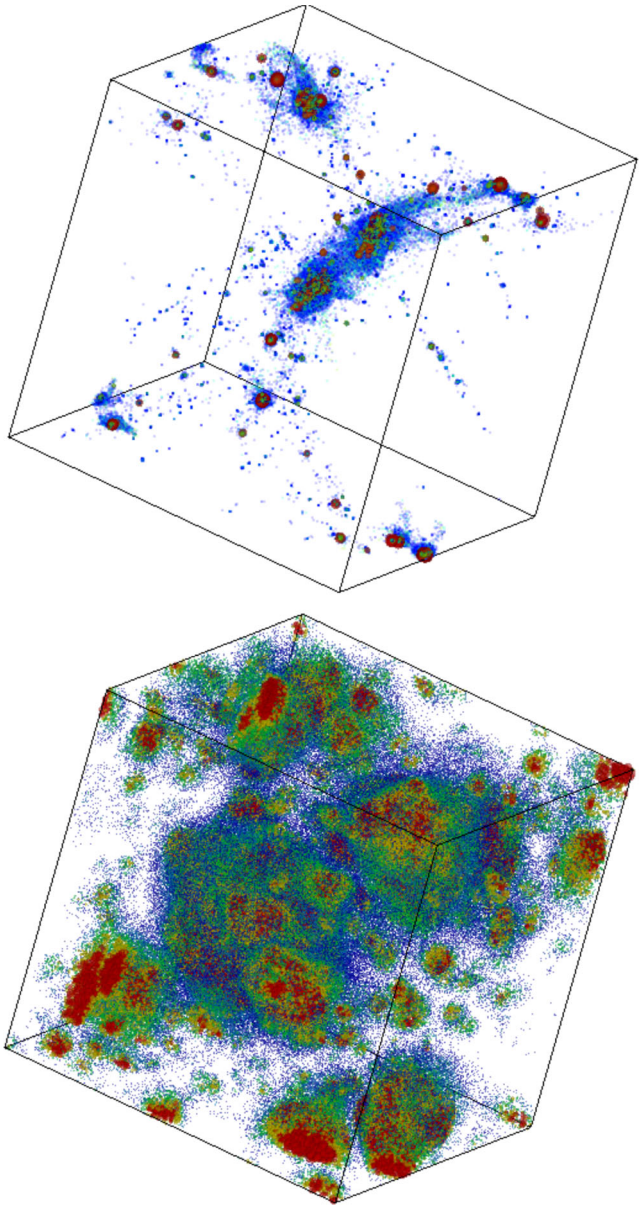

Figure 3. Top: The dot plot of a subset of particles with $n_{\rm ff} \geq 6$ in the simulation of $1/h$ Mpc box in the ΛCDM cosmology at $z = 0$. The figure illustrates the densest regions of the simulation. Bottom: The subset of particles shown in the top panel is plotted in Lagrangian space. The sizes of dots are scaled by $n_{\rm ff}$ and the colours change with the growth of $n_{\rm ff}$ from blue to red.

significant decreasing of noise resulting in remarkable sharpening of the contours. It also results in reducing of the heights of the peaks. For instance the height of the major peak is reduced from 616 in the raw field to 551, 474 and 446 in the filtered field which is not surprising because the peaks have steep heads. However, the intricate nested substructure of the halo remains mostly intact. This suggests that the numerical noise is not too bad and the flip-flop field it reasonably robust.

4.2 An example of substructure in the highest flip-flop peak

In this section, we focus on the highest flip-flop peak ($\max(n_{\rm ff}) = 616$ at $a = 1$) in a set of the peaks selected by the condition $n_{\rm ff} \geq 20$. It corresponds to one of dynamically most evolved haloes. Fig. 6 shows the three-dimensional structure of the peak in six panels starting with the contour at $n_{\rm ff} = 20$ in the top left panel. In each of five remaining panels, we plot two contours: one in grey colour shows the same contour as in the top left panel and the other at steadily increasing levels $n_{\rm ff} = 42$, 67, 100, 130, 162 respectively. One can clearly see a rich nesting structure of the peak.

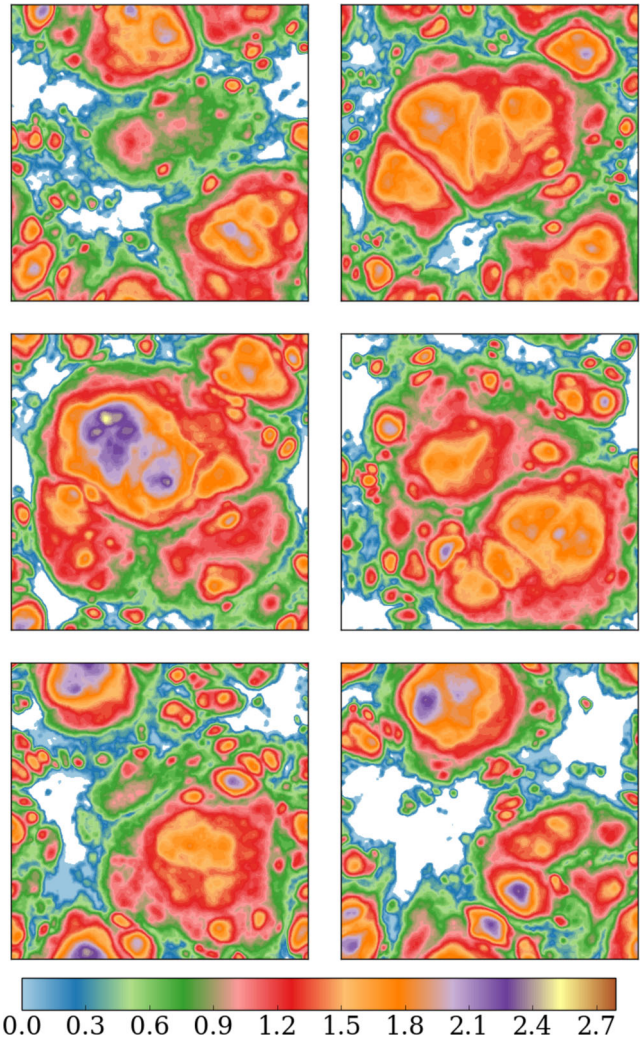

Figure 4. Six panels display *XZ* – slices of the flip-flop field filtered with Gaussian widths of 1.0 in units of the interparticle distance in Lagrangian space. The slices are approximately equally spaced along *Y*-axis and ordered from top left to right to bottom. The colour bar legend shows $\log_{10}(n_{\rm ff})$. The middle left panel shows the slice through the largest peak of the flip-flop field. The regions with $n_{\rm ff} = 0$ are shown in white.

5 STATISTICAL PROPERTIES OF THE FLIP-FLOP FIELD

First, we briefly discuss some of global statistical properties of the flip-flop field in comparison with density and gravitational potential fields. There is a subtlety in such a comparison. We compute the flip-flop field on particles therefore it is a Lagrangian field. The density can also be computed on particles or in tetrahedra of the tessellation of the Lagrangian submanifold as described in Shandarin et al. (2012) and Abel et al. (2012), but this would be the density

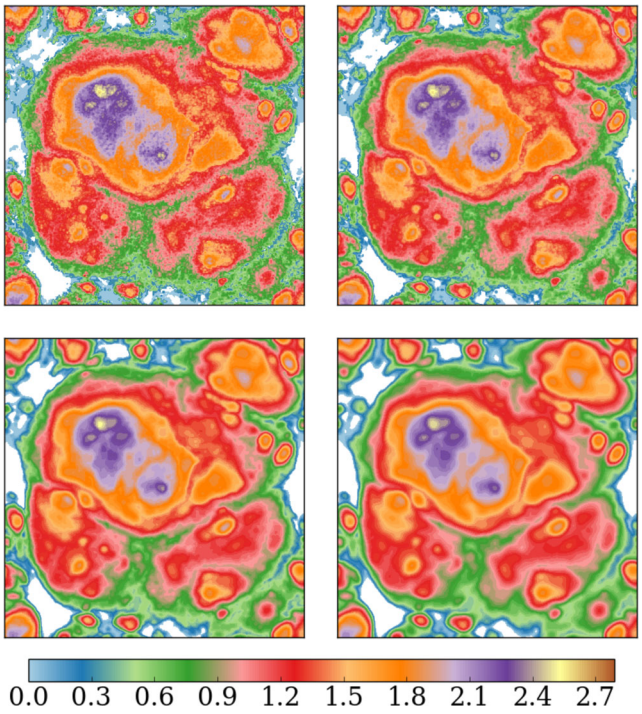

Figure 5. Four panels show the effect of smoothing of the flip-flop field in 256^3 simulation. The two-dimensional slice passing through the highest peak shows the raw field in the top left panel and filtered fields with Gaussian widths of 0.5, 1.0 and 1.5 in units of the interparticle distance in Lagrangian space in top right, bottom left and bottom right panels respectively. The legend of the colour bar shows $\log_{10}(n_{\rm ff})$. The regions with $n_{\rm ff} = 0$ are shown in white.

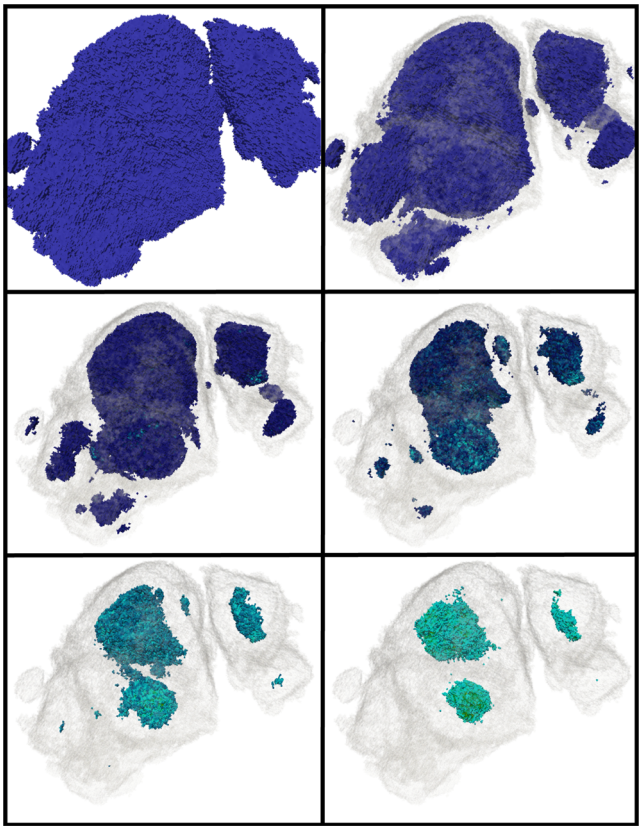

Figure 6. The substructure in the highest peak of the 256^3 simulation with $\max(n_{\rm ff}) = 616$ is shown as a set of six isocontours in 3D. From top left panel to down right panel colour contours are respectively: $n_{\rm ff} = 20$, 42, 67, 100, 130, 162. Five panels also show the grey shade of the contour at $n_{\rm ff} = 20$ shown in the top left panel in blue.

in separate streams not the total density in Eulerian space. Here we would like to compare the flip-flop field with commonly used density field computed in Eulerian space. However the interpolation of the Eulerian density to particles is not uniquely defined procedure. Since our simulations are done with GADGET code, we use smoothed particle hydrodynamics (SPH) densities and potentials computed on particles available in standard outputs of the code. We caution that other methods of computing density on particles may produce somewhat different results from reported here although we do not anticipate a substantial difference.

We start with making a list of obvious differences between three fields in question:

(i) The number of flip-flops is unambiguously defined field in Lagrangian space; it is determined by the count of sign changes of $\det[\partial x_i(q)/\partial q_j]$ on each particles in Lagrangian space. However one can define two different types of the density field in Eulerian space: one is determined by the total DM mass in a volume element $\rho_{\rm t}(\boldsymbol{x})\mathrm{d}^3x$ and the other by the DM mass in every stream in the volume element $\rho_i(\boldsymbol{x})\mathrm{d}^3x$ where i is the index of a stream, with an obvious relation: $\rho_{\rm t}(\boldsymbol{x}) = \sum_i \rho_i(\boldsymbol{x})$. The total density $\rho_{\rm t}(\boldsymbol{x})$ is always a single-valued function but $\rho_i(\boldsymbol{x})$ is a multivalued function in the regions with multistream flow. The densities in the streams become the density field in Lagrangian space because each stream i in dx has a unique progenitor dq_i in Lagrangian space. The total DM density in Eulerian space cannot be unambiguously assigned to a set of Lagrangian regions dq_i overlapping in dx. The SPH density or potential on particles in N-body simulations of a collisionless medium is only one of many feasible approximate maps of Eulerian fields $\rho_{\rm t}(\boldsymbol{x})$ and $\Phi(\boldsymbol{x})$ to Lagrangian space because $\boldsymbol{q}(\boldsymbol{x})$ is not a single-valued function in the multistream regions.

(ii) The flip-flop field is a discrete field with positive integral values while both density and potential are continuous fields apart from the discreteness related to the grid.

(iii) Both the flip-flop and density fields are positively defined while potential can be both positive and negative.

(iv) The number of flip-flops monotonically grows with time at every particle while both the density and potential do not because some particles can move back and forth between high- and low-density environments as well between regions with high and low potentials.

5.1 Cumulative probability functions

Fig. 7 shows the fractions of particles with densities above the threshold $\rho_{\rm th}$ in the range of $0.001 \le \rho_{\rm th} \le 15$ and the fractions of particles with the number of flip-flops above the threshold $n_{\rm th}$ in the range $1 \le n_{\rm th} \le 50$ in the top and bottom panels respectively. The ranges correspond approximately 90 per cent of lowest values of the fields in both plots. The plots of the cpfs showing the highest 1 per cent of the values are shown in Fig. 8. The cpf is shown for both 128^3 and 256^3 simulations.

The figures demonstrate that the cpf of the flip-flop field is considerably more regular function of the cosmological epoch and the

[ht]

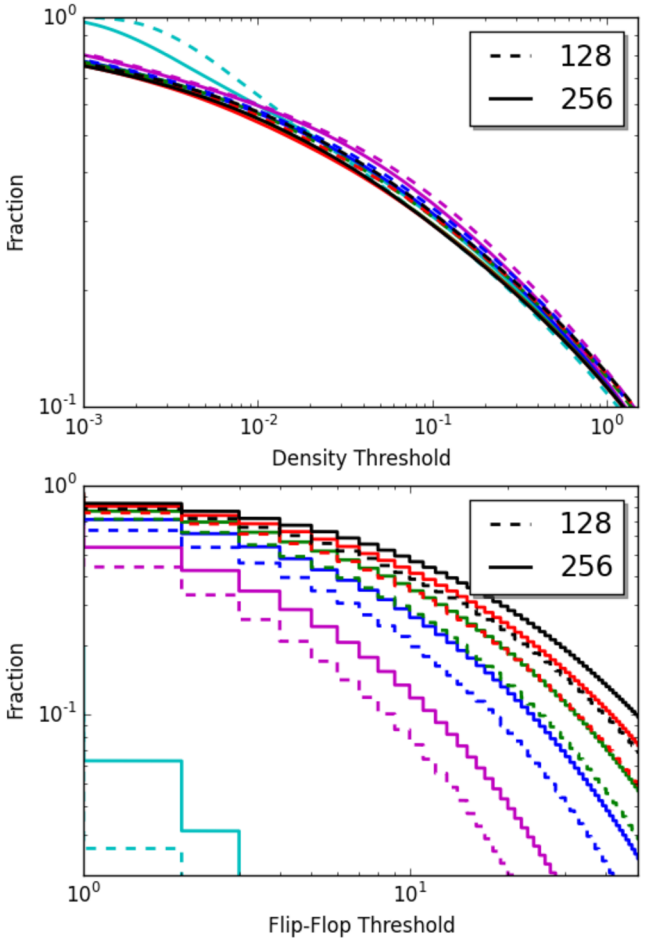

Figure 7. The cumulative probability functions of the lowest 90 per cent of density (top) and flip-flop (bottom) fields are shown at six epochs: $a = 0.026$, 0.058, 0.129, 0.242, 0.493, 1.000 in 128^3 and 256^3 simulations. Colours in the order of epochs are: cyan, magenta, blue, green, red and black.

size of the simulation than the density in Lagrangian space.[5] The flip-flop cpf monotonically increases with time and with the mass resolution of the simulation. The density cpf does show much lesser dependence on both the size of the grid and the epoch.

5.2 The growth of the web mass

The fraction of mass experienced the strongest non-linear event – flip-flop – monotonically increases with time. The slope of the power spectrum of the linear density perturbations in the range from the Nyquist wavelength $L_{\rm Ny} \approx 16\,h^{-1}$ kpc or $\approx 8\,h^{-1}$ kpc in 128^3 or 256^3 simulation respectively to the size of the simulation box is quite steep. Therefore, the fraction of mass reached a strong non-linear regime when a fluid element experiences a flip-flops grow very fast. The blue curves in Figs 9 and 10 show the fractions of mass experienced the first flip-flop between the output times equally spaced on the $\log_{10}(a)$ scale from approximately 0.023 to 1. The

[5] The outputs of the Gadget code include the density and potential computed on the simulation particles and therefore they are Lagrangian fields similar to the coordinates and velocities of the particles.

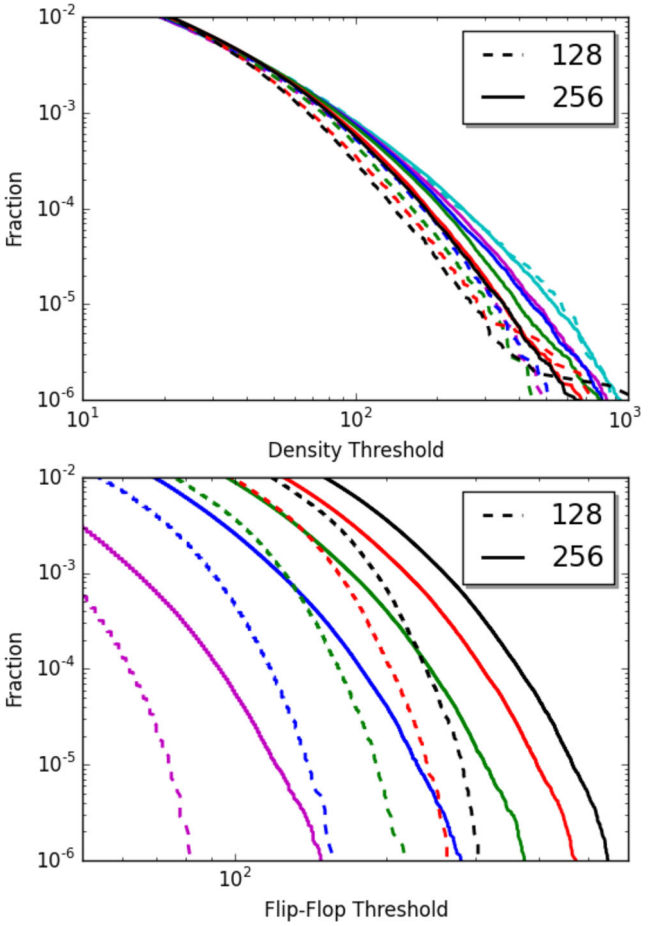

Figure 8. Same as Fig. 7 except that these are the cpfs of the highest 1 per cent of the values of the fields are shown.

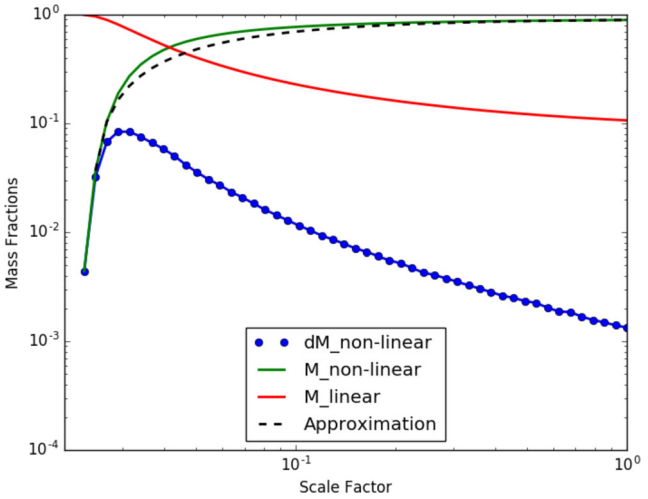

Figure 9. 128^3 simulation. A blue line with dots shows the fractions of mass experienced the first flip-flop between (i-1)-th and i-th outputs of the N-body code as a function of a_i. The green curve shows the accumulation of mass experienced at least one flip-flop by a_i while the red curve demonstrates the mass fractions that have not experienced flip-flops at all by a_i. The dashed line in black shows a crude analytical approximation to the green line.

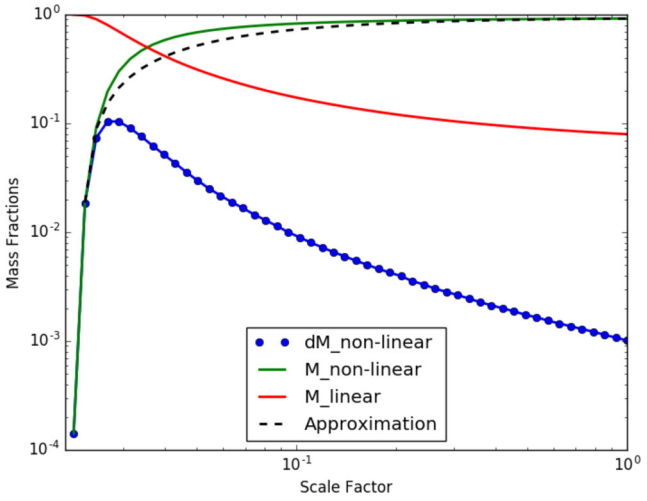

Figure 10. 256^3 simulation. Notations are the same as in Fig. 9.

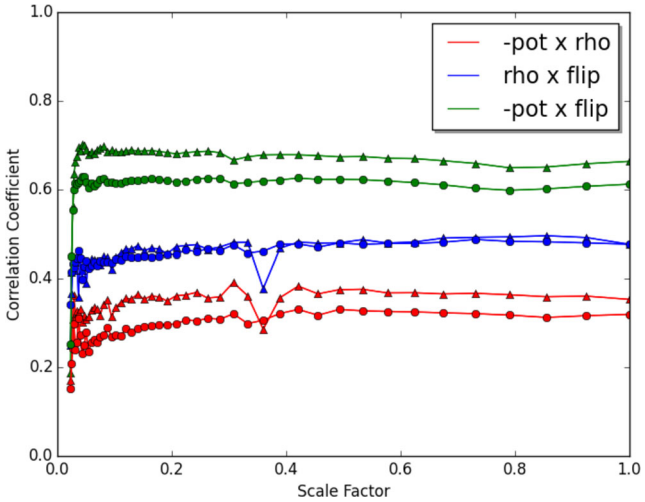

Figure 11. Correlation coefficients of all pairs of three Lagrangian fields in Lagrangian space: negative potential (−pot), density (rho) and flip-flop (flip) as a function of the scalefactor. Triangles and circles correspond to the simulations with 128^3 and 256^3 particles respectively.

green lines show the growth of the mass fraction experienced at least one flip-flop by a_i while the red lines show the decrease of the mass fraction that did not experience even a single flip-flop. After reaching about a third of the total mass at $a \approx 0.03$ the growth of the mass in the non-linear regime (blue curves) is steadily reducing reaching about 0.1 per cent by the present time ($a = 1$). The total mass in the particles never experienced flip-flops has dropped to about 10 per cent or 8 per cent in the 128^3 or 256^3 simulations respectively.

The black dashed line is a crude analytic approximation of the growth of the mass fraction reached non-linearity by a function with two free parameters:

$$f(a) = C_1 - \frac{C_2}{a}.$$

The parameters are chosen to make the approximation curve to pass through the second and last points of the green curve obtained in the N-body simulations. The approximation obviously is far from perfect and is not intended for further use. It still may be useful because it demonstrates a very fast growth of the mass in the dark matter web, which is probably faster than exponential rate between $a = 0.023$ and $a = 0.03$. In the 128^3 simulation $C_i = (0.022, 0.92)$ and in the 256^3 simulation the are $C_i = (0.021, 0.94)$ showing that the difference between two simulation is noticeable but quite small.

5.3 Correlation properties

In this and following section, we present the results of comparison of three fields: flip-flop, density and gravitational potential. As we mentioned earlier, the flip-flop is naturally defined in Lagrangian space on particles. The density and potential fields are naturally defined in Eulerian space. However, GADGET provides them on particles which we consider a particular mapping of the Eulerian fields to Lagrangian space. It is by no means unique but we have it free and thus we compare the three fields as Lagrangian fields.

5.3.1 Correlations between the pairs of different fields at the same epoch

It is expected that the density, potential and flip-flop fields correlate with each other since the higher densities and higher numbers of flip-flops tend to be more frequent in the regions of negative potential.

In order to quantify these anticipations, we evaluate the correlation coefficients of the fields in question at a number of epochs in both 128^3 an 256^3 simulations. We use the standard definition of the correlation coefficient between two functions X and Y:

$$\mathrm{corcoef}(X, Y) = \frac{E[(X - < X >)(Y - < Y >]}{\sigma_X \sigma_Y},$$

where E and σ mean the expected value and standard deviation respectively. The flip-flop, density and potential are defined on the particles of the simulation as described before. Therefore, it is a particle-by-particle or in other words pixel-by-pixel correlation in Lagrangian space. Fig. 11 shows each correlation coefficient as a function of a scalefactor. They exhibit a remarkably weak evolution if any with time. The highest correlation is between the potential and flip-flop fields, while the lowest between potential and density fields. Both become weaker with the growth of the mass resolution while the correlation coefficient of the density and flip-flop fields seems to be very similar in both simulations. The correlations between the density and flip-flop fields is intermediate for these simulations and do not show any dependence on the size of the simulation. Its magnitude being around 0.45 suggests that the fields seem to have something in common with each other but they are not very similar. Both dependences on the size of the simulation look natural. Adding small-scale power to the initial perturbations in the 256^3 simulation results in reducing the scale of the both density and flip-flop fields without a significant effect on the scale of the potential.

5.3.2 Correlations between the pairs of the same field taken at different epochs

Here we present the correlation coefficient of the same field taken at two different epochs: corcoef$[f(a_i), f(a_{\rm ref})]$ where $f = [\rho, \phi, n_{\rm ff}]$ i.e. it is either density or potential of flip-flop field computed on particles and therefore are Lagrangian fields. We selected two reference epochs: $a_{\rm ref\,1} = 1$ and $a_{\rm ref\,0.1} = 0.1$. In both cases, we compute the correlation coefficients with all previous stages $a_i < a_{\rm ref}$. In order to emphasize how close to unity the correlation coefficient of the flip-flop field is we plot $\log_{10}(1 - \mathrm{corcoef}(f_i, f_k))$ instead of $\log_{10}(\mathrm{corcoef}(f_i, f_k))$ in Fig. 12.

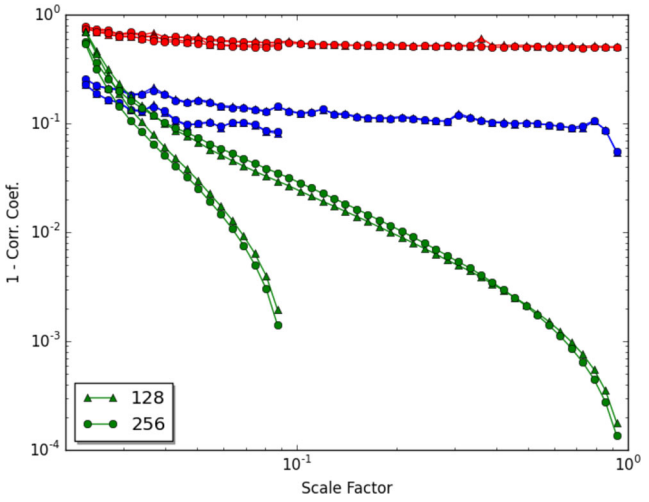

Figure 12. Correlation coefficient of the density $\xi_{\rho\cdot\rho}$ (red), potential $\xi_{\varphi\cdot\varphi}$ (blue) and flip-flop $\xi_{\mathrm{ff}\cdot\mathrm{ff}}$ fields at $a = 1$ (long curves) and $a = 0.1$ (short curves) with corresponding fields at all previous stages. In order to see how close to unity $\xi_{\mathrm{ff}\cdot\mathrm{ff}}$ is, we plot the logarithm of its difference from unity. The curves are shown for both $N_{\mathrm{p}} = 128$ (triangles) and 256 (circles) simulations.

It is no surprise that all fields correlate stronger when two epochs get closer to each other. However, the strength of the correlation as well as dependence on the epoch a_i are substantially different between all three fields. The density correlation coefficient shown in red is the lowest and the most stably growing from about 0.2 at the largest separation of the epochs to about 0.5 for the closest epochs. There is practically no difference between 128^3 and 256^3 simulations and barely noticeable difference between two reference epochs $a_{\mathrm{ref}\,1} = 1$ and $a_{\mathrm{ref}\,0.1} = 0.1$. The potential correlation coefficient shown in blue is significantly higher with the range from about 0.75 to 0.95 with distinct difference between two reference epochs $a_{\mathrm{ref}\,1} = 1$ and $a_{\mathrm{ref}\,0.1} = 0.1$.

The overall highest correlation coefficient and the greatest difference between two reference epochs is displayed by the flip-flop field. Although it is similar to the density correlation coefficient at the largest separation of the epochs, it grows very quickly above 0.9 at $a_i \approx 0.03$ and then above 0.99 at $a_i \approx 0.05$ and at $a_i \approx 0.2$ for the reference epochs $a = 0.1$ and $a = 1$ respectively. Such a small difference of the correlation coefficient with unity suggests that the difference of the fields at the corresponding epochs is mostly due to a constant factor. It means that the geometry of the flip-flop field does not evolve much after some epoch which means in turn that the peak structure in the flip-flop field keeps the record of the formation of the haloes even after they experienced mergers with other haloes.

5.4 Comparison of the flip-flop, density and potential fields in Lagrangian space

Here we continue to consider both densities and potentials on particles and therefore treat them as Lagrangian fields. We computed the ratios of a field at chosen epoch a_i to it at a reference epoch $a_i < a_{\mathrm{ref}}$: $R^{(F)}_{i,\mathrm{ref}} = F(\boldsymbol{q}, a_i)/F(\boldsymbol{q}, a_{\mathrm{ref}})$, where F is either the flip-flop or density or potential field and a_{ref} is either 0.1 or 1. Then we estimated the mean, median and standard deviations of the ratio fields. Fig. 13 shows the results for all three fields at 47 scalefactors in the range from 0.02 to 0.92 when the reference field was chosen at $a_{\mathrm{ref}} = 1$ and at 18 scalefactors in the range from 0.02 to 0.087 when the reference field was chosen at $a_{\mathrm{ref}} = 0.1$. The mean and std

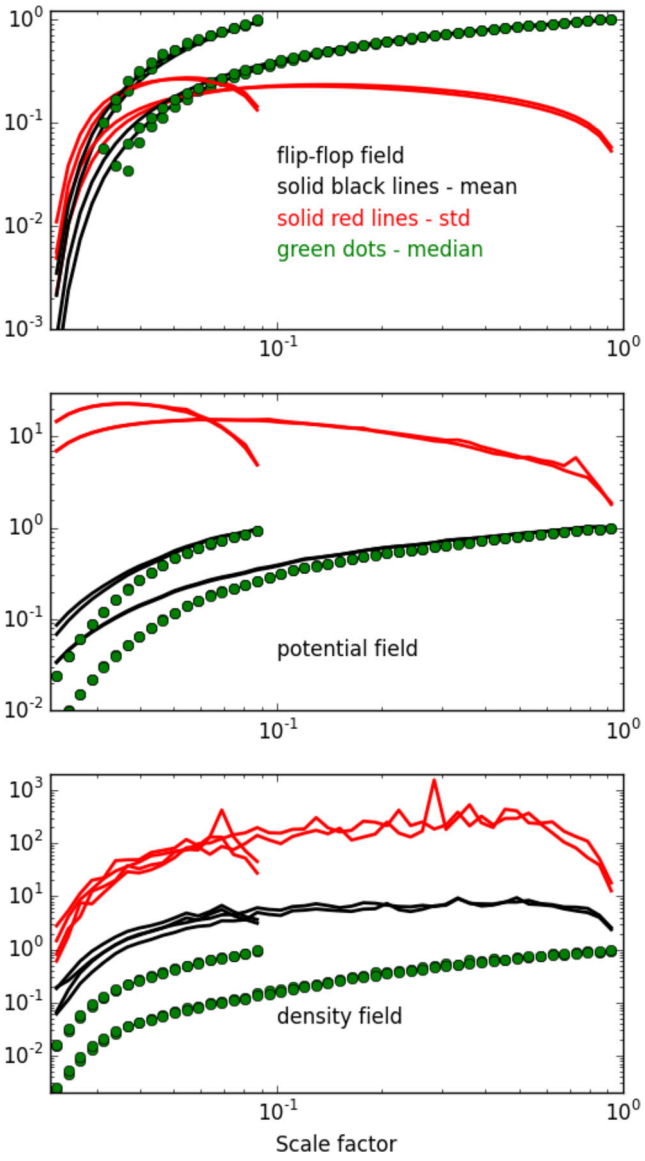

Figure 13. The mean, std and median of the ratios of the field at the scalefactors shown on the horizontal to the same field at the reference epoch. Two sets of curves correspond to two reference epochs $a_{\mathrm{ref}} = 0.1$ (short curves) and $a_{\mathrm{ref}} = 1$ (long curves). The curves corresponding to 128^3 and 256^3 simulations noticeably different only for mean and std values of the density field shown in the bottom panel.

values are shown in black and red colours respectively in three panels: flip-flop field – in the top, potential – in the middle and density – in the bottom panels of Fig. 13. The median values of $R^{(F)}_{i,\mathrm{ref}}$ are shown by green dots.

5.4.1 *Flip-flop field (top panel of Fig. 13)*

For the majority of the epochs a_i, the values of $\sigma(R^{(\mathrm{ff})}_{i,\mathrm{ref}})$ is significantly smaller than the mean and median values that are practically the same: $\sigma(R^{(\mathrm{ff})}_{i,\mathrm{ref}}) \ll \mathrm{mean}(R^{(\mathrm{ff})}_{i,\mathrm{ref}}) = \mathrm{median}(R^{(\mathrm{ff})}_{i,\mathrm{ref}})$. It demonstrates that the flip-flop field grows in very orderly manner with stochastic effects being quite small.

5.4.2 Potential field (middle panel of Fig. 13)

The difference between mean($R^{(\varphi)}_{i,\mathrm{ref}}$) and median($R^{(\varphi)}_{i,\mathrm{ref}}$) are more distinct at large separations of the epochs and significantly diminishes as the epochs get closer. The most conspicuous difference of $R^{(\varphi)}_{i,\mathrm{ref}}$ from $R^{(\mathrm{ff})}_{i,\mathrm{ref}}$ is a large value of std at all epochs $\sigma(R^{(\varphi)}_{i,\mathrm{ref}}) \gg \mathrm{mean}(R^{(\varphi)}_{i,\mathrm{ref}}) \approx \mathrm{median}(R^{(\varphi)}_{i,\mathrm{ref}})$ with the lowest value of about twice of the mean at the smallest separation from $a_{\mathrm{ref}} = 1$.

5.4.3 Density field (bottom panel of Fig. 13)

The evolution of $R^{(\rho)}_{i,\mathrm{ref}}$ is essentially stochastic: $\sigma(R^{(\rho)}_{i,\mathrm{ref}}) \sim 100 \times \mathrm{mean}(R^{(\rho)}_{i,\mathrm{ref}})$ and $\sigma(R^{(\rho)}_{i,\mathrm{ref}}) \sim 1000 \times \mathrm{median}(R^{(\rho)}_{i,\mathrm{ref}})$ making both rather useless.

Summarizing Section 5.4 we would like to stress the qualitative difference between evolutions of the flip-flop and SPH density and gravitational potential fields evaluated on particles. The flip-flop evolves in a remarkably orderly manner with mean and median of the ratios $n_{\mathrm{ff}}(\boldsymbol{q}, a_i)/n_{\mathrm{ff}}(\boldsymbol{q}, a_{\mathrm{ref}})$ being almost exactly equal and std being much smaller. It is a strong evidence that the geometry of the flip-flop field in Lagrangian space evolves very little. On the contrary the evolution of the potential and especially density field is almost stochastic. While the both the mean and median of the ratios of the both fields monotonically increase with time approaching unity as a_i is approaching to the corresponding a_{ref} as expected the standard deviations are considerably greater at all epochs making the mean and median values useless.

5.5 A unique feature of the evolution of the flip-flop field

Discussing a simple one-dimensional halo in Section 1, we argued that the closer the orbit of a fluid element to the centre of the halo the shorter its characteristic time. It means that the earlier the fluid element collapsed for the first time the greater its counts of flip-flops at later epochs. A similar trend prevails in generic haloes with substructures in three dimensions although it is not exact but valid in statistical sense as we describe below. Fig. 14 provides a quantitative illustration of this assertion.

For the plot we binned particles according to their gains in flip-flops counts $\Delta n_{\mathrm{ff}} = n_{\mathrm{ff}}(a_{i+1}) - n_{\mathrm{ff}}(a_i)$ at every output stage a_i of the 256^3 simulation. Then we computed the mean number of flip-flops mean[$n_{\mathrm{ff}}(a_i)$], standard deviation $\sigma[n_{\mathrm{ff}}(a_i)]$ and the fractions of the particles in 13 bins with $0 \le \Delta n_{\mathrm{ff}} \le 12$. Thirteen lines in the top panel show mean[$n_{\mathrm{ff}}(a_i)$] for each bin in descending order of Δn_{ff} from top to bottom. The middle panel shows $\sigma[n_{\mathrm{ff}}(a_i)]$ for all bins, the order of bins is same as in the top panel.[6] The bottom panel shows the fraction of particles in every bin. Obviously the lines in this panel are in the reversed order of two top panels. The largest fraction of particles gets the smallest raise at all times – the bottom red line in the top panel corresponding to the top line in the bottom panel.

Although not every particle always remains in the same bin, the particle mobility between bins is very limited. The bins fairly well separated as the plot of $\sigma[n_{\mathrm{ff}}(a_i)]$ in the middle panel shows. The top panel shows that the particles in the higher bin having a greater raise Δn_{ff} by design have on average higher mean[$n_{\mathrm{ff}}(a_i)$]. Thus the particles that gained superiority in the number of flip-flops at early non-linear stages on average remain among the leaders at later times. Therefore, we conclude that the geometrical pattern of peaks and valleys in the flip-flop field does not change much with time. This is in agreement with Fig. 2 showing the evolution of the flip-flop field in two-dimensional simulation.

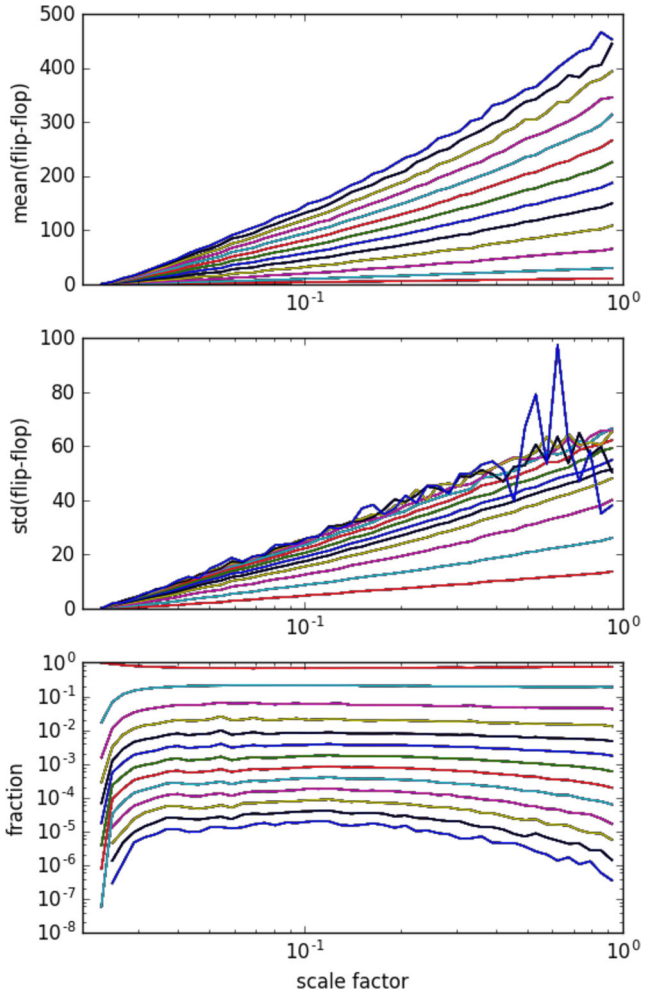

Figure 14. Conditional statistics of the flip-flop field as a function of the scalefactor. The particles are binned according to the change of the number of flip-flops between the outputs $\Delta_{\mathrm{ff}} = n_{\mathrm{ff}}(a_{i+1}) - n_{\mathrm{ff}}(a_i)$. The curves are in the range $0 \le \Delta_{\mathrm{ff}} \le 12$ from the bottom to top in top two panels and in the reverse order in the bottom panel. The panels show the mean, std and fraction of the particles in each bin from top to bottom.

Fig. 15 provides an additional evidence for the conclusion of the previous paragraph. It shows the histograms of mass fractions in the bins of the final counts of flip-flops at $z = 0$ (i.e. $a = 1$) in nine sets of particles. The particles in the first set (about 1.9 per cent) experienced first flip-flopping at $z > 42.6$; it is shown by the blue curve on the right. All particles with $n_{\mathrm{ff}}(z = 0) > 400$ and most of particles with $250 < n_{\mathrm{ff}}(z = 0) < 400$ are members of this set. The green histogram on the right shows 7.4 per cent of particles that experienced first flip-flopping between $z = 42.6$ and $z = 39.3$ and so forth.

The figure clearly demonstrates that the particles experienced first flip-flopping at $z > 36.2$ dominate in the highest counts of flip-flops, say $n_{\mathrm{ff}} > 50$, at $z = 0$. They make less than 20 per cent of the total mass or less than 22 per cent of all particles experienced at least one flip-flop as Fig. 15 shows. Most of these particles are obviously in a close proximity to the highest peaks of the final flip-flop field.

[6] Large fluctuations of $\sigma(n_{\mathrm{ff}}(a_i))$ for a couple of the highest bins are caused by very limited statistics as the bottom panel shows.

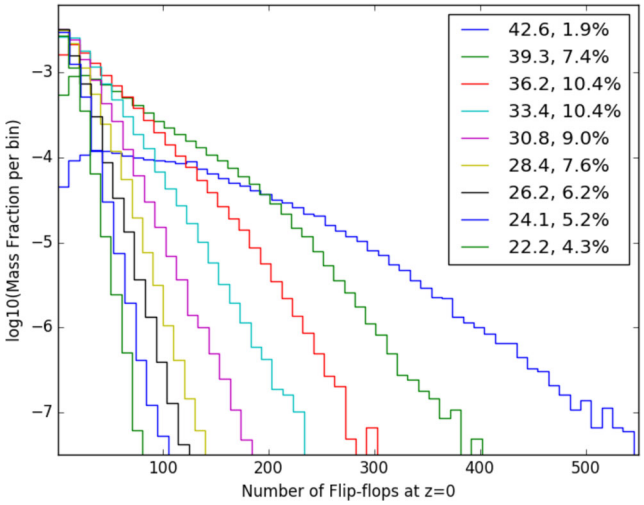

Figure 15. The logarithm of the fraction of mass in bins with the number of flip-flops at $z = 0$ shown on the horizontal. Nine histograms correspond to the particles experienced first flip-flopping between that redshift and the previous redshift listed in the legend. For example, the second (green) curve from the right corresponds to the particles that experience the first flip-flopping at $42.6 > z > 39.3$. The second column in the legend shows the total fractions of the mass in the particles satisfying the above criterion.

5.6 The number of peaks

Now we will turn to the issue of the number of peaks in the flip-flop field. It is worth stressing that here we do not mean the points of maxima of $n_{\rm ff}$ in Lagrangian space but rather the regions of the field with the number of flip-flops above a certain level. More exactly, we will look at the evolution of the excursion set in the flip-flop field at all 50 output epochs. The peaks and there structures represent the major interest because they are associated with the haloes and subhaloes.

Figs 16 and 17 show the number of peaks as a function of the filling factor at every output epoch in the 128^3 and 256^3 N-body simulations. We count peaks with three different sizes: >100, >50 and >25 particles. The left-hand panels show earlier stages $a < 0.1$ characterized by relatively fast evolution and the right-hand panels show later stages with $0.1 \leq a \leq 1$ when the evolution is considerably slower. The number of peaks increases with the growth of the filling factor as the threshold is decreasing and reaches a broad maximum around FF ≈ 0.2. Then at greater filling factors many peaks begin to merge with each other and therefore their number decreases.

It is remarkable that at $a > 0.1$ the curves corresponding to different scalefactors a are packed quite tightly forming a relatively narrow strip. This behaviour is quite different from that at earlier stages $a < 0.1$. There is no much difference between the 128^3 and 256^3 simulations apart from the number of peaks, which is expected. Generally it is in a good agreement with the results described in previous sections and confirms that the geometry of the flip-flop landscape does not evolve much at $a > 0.1$

6 COMPARISON WITH AHF HALOES

We are suggesting that the peaks of the flip-flop field computed in Lagrangian space are directly related to the DM haloes and subhaloes. If it is true then the maxima of the flip-flop field must be inside of the both haloes and subhaloes identified in Eulerian space.

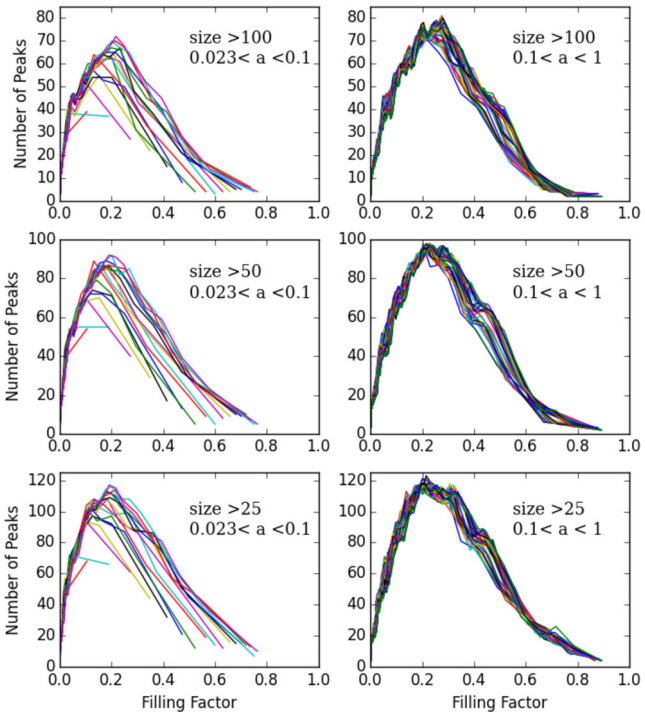

Figure 16. Number of peaks as a function of filling factor is plotted for every output of the simulation with 128^3 particles. The counts for outputs at early stages $a < 0.1$ are shown on the left and the rest are shown on the right. The counts are made for three thresholds of the size as shown in the panels.

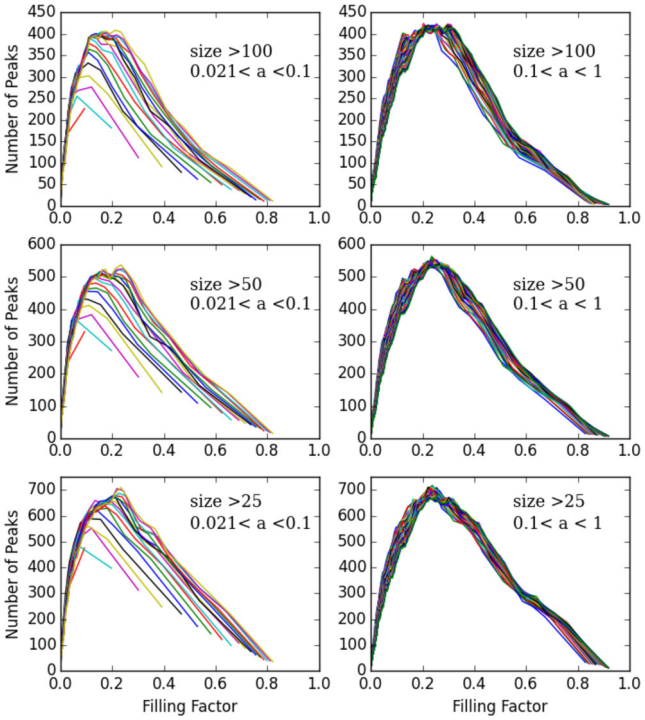

Figure 17. Same as in Fig. 16 but for the simulate with 256^3 particles.

As we mentioned in Section 1, a number of different methods and techniques have been suggested to identify and study haloes, in particular DM haloes. We studied a set of haloes obtained by a publicly available Amiga Halo Finder or AHF (Gill, Knebe &

Gibson 2004; Knollmann & Knebe 2009). The AHF code provides the haloes and subsaloes with more than 20 particles.

The progenitor of a halo or subhalo in Lagrangian space typically represents a set of connected particles on a regular grid. The simplest way to check our proposition is to find the maxima of the flip-flop field in Lagrangian space then map them to Eulerian space and check their distances from the centres of the AHF haloes.

There are three basic types of connectivity of the particles on a cubic grid in Lagrangian space which can be used for numerical finding of maxima: each particle can be connected to 6, 18 or 26 closest neighbours. A reasonable algorithm for searching maxima requires the comparison of the value of a function on a particle with that on its 26 closest neighbours. Thus, it requires that the progenitor of the halo to occupy at least a 3 by 3 by 3 cube on the grid and therefore must consist of at least 27 particles. However, the shapes of the Lagrangian progenitors of small AHF haloes often are significantly different from a simple cubical configuration. To be on a safe side, we restricted our statistical analysis to the haloes with more than a hundred particles and the maximum flip-flop greater than 10. We start with the analysis of a few statistics of sabhaloes within the largest by mass AHF halo in 256^3 simulation.

6.1 Statistics

In order to quantitatively address the question of how close are the maxima of the flip-flop field to the virial centres of the AHF haloes or subhaloes, we selected those with $N_{\rm part.} \geq 100$ and $n_{\rm ff,max} \geq 10$, totally 2069 i.e. roughly 20 per cent of all AHF haloes with more than 20 particles. For brevity we will refer to them as haloes in the rest of this section. For the selected haloes, we computed the cumulative probability function of the ratios $R_{\rm max}/R_{\rm vir}$ where $R_{\rm max}$ is the distance of the maximum of the flip-flop field from the centre of the corresponding AHF halo in Eulerian space. In order to find the position of each maximum, we selected all the particles with the largest value of flip-flop, i.e. the global maximum in each set of particles comprising a halo identified by the AHF algorithm. In most of haloes it was just a single particle; however, since the number of flip-flops is integral on rare occasions more than one particle had the largest count of flip-flops,[7] in such a case we took the mean position of the particles with the maximum count of flip-flops. Then for each position of the maximal count of flip-flops, we computed the distance from the virial centre of the corresponding halo.

The cumulative probability function of the ratios $R_{\rm max}/R_{\rm vir}$ is displayed in Fig. 18. For convenience, we show three horizontal lines marking 1, 5 and 10 per cent of particles with highest values of the ratio $R_{\rm max}/R_{\rm vir}$. The vertical lines show the corresponding values of the ratio. Thus $R_{\rm max}/R_{\rm vir} < 0.54, 0.69, 0.92$ in 90 per cent, 95 per cent and 99 per cent of the haloes respectively.

In order to show the correlation between the maxima of flip-flops, $n_{\rm ff,max}$, ratios $R_{\rm max}/R_{\rm vir}$ and AHF masses i.e. the number of particles, we made scatter plots of three pairs of these parameters in Fig. 19. The top panel shows the maxima of flip-flop versus the number of particles in the halo. Haloes with more than about 200 particles clearly display the tendency of the flip-flop maximum to grow with the growth of their masses. The ratio $R_{\rm max}/R_{\rm vir}$ obviously decreases with the growth of the halo mass as quite clearly shown in the middle panel. The bottom panel exhibits similar tendency with the growth of the flip-flop maximum of the halo at $n_{\rm ff,max} \gtrsim 20$, which qualitatively follows from the correlations observed in the top and middle panels. For haloes with $N_{\rm p} \lesssim 200$ or/and $n_{\rm ff,max} \lesssim 20$, the both correlations become more noisy.

[7] This happens mostly in haloes with fewer than a hundred particles but sometimes it also occurred in the selected 'large' haloes as well.

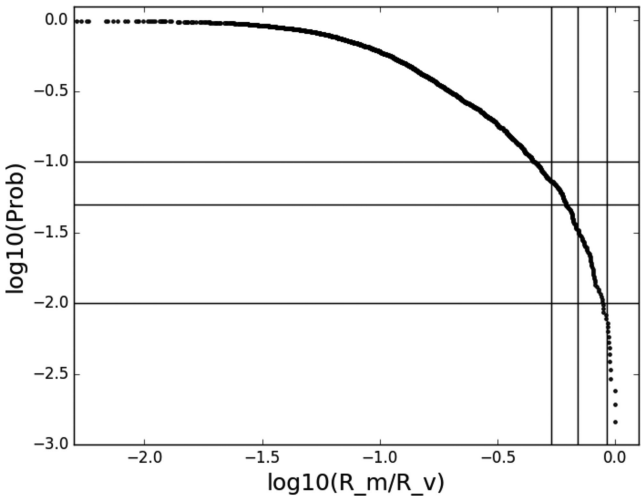

Figure 18. Cumulative probability function of the ratio $R_{\rm max}/R_{\rm vir}$. Three horizontal lines show 1, 5 and 10 per cent levels and the vertical lines show the corresponding values of $R_{\rm max}/R_{\rm vir}$ which are 0.92, 0.69 and 0.54 respectively. For example, in 90 per cent of haloes the distances of the flip-flop maxima are less than 0.54 of the virial radius.

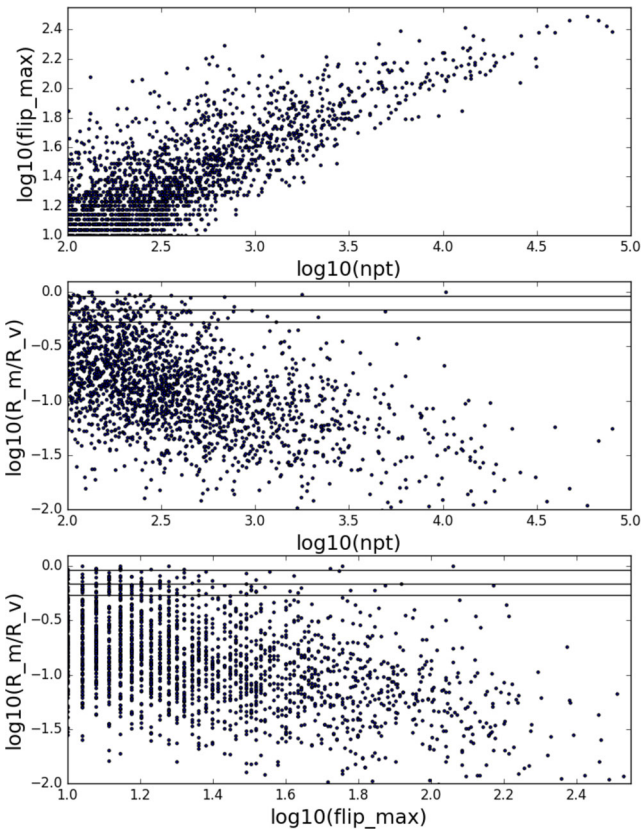

Figure 19. The top two panels show the flip-flop maxima and the ratio $R_{\rm max}/R_{\rm vir}$ respectively versus the number of particles in selected AHF halo/subhaloes. The bottom panel shows the ratio $R_{\rm max}/R_{\rm vir}$ versus the maximum of the flip-flop field in the haloes. Horizontal lines in two lower panels correspond to the vertical lines in Fig. 18, i.e. $R_{\rm max}/R_{\rm vir} = 0.92, 0.69, 0.54$

The horizontal lines in the middle and bottom panels correspond to the vertical lines in Fig. 18. Although they show that the largest ratios of $R_{\rm max}/R_{\rm vir}$ are characteristic for small haloes with low maxima of flip-flop field but the most of them have a clear maximum of the flip-flop field within a sphere centred on the virial centre and the radius less than about a half of the virial radius. It is worth stressing that the haloes with fewer than a hundred particles are probably seriously affected by numerical noise in this simulations.

7 THE EVOLUTION OF THE HIGHEST FLIP-FLOP PEAK

7.1 Illustration

Fig. 20 shows two orthogonal projections of the AHF halo mentioned in Section 6 (see Fig. 6). Two projections help a little to reduce the obscuring effect due to projection. The halo is shown as a sphere of the viral radius. It also shows the virial spheres of sabhaloes with more than a hundred particles and the maximum of flip-flop value greater than a hundred, totally 74 out of 173 found in this halo by AHF finder with more than 20 particles. The centres of the virial spheres are shown as white dots. The particles with the maxima of the flip-flop field are shown by small colourful spheres where both the radii and colours reflect the magnitude of the flip-flop maxima. Colours from dark blue to red correspond to the ascending order of the heights of the maxima in the range from 17 to 402, Generally both the colourful spheres and white dots are clearly seen in one or the other projection. However in a few cases the spheres obscure the centres of the virial spheres in both projections. The largest red sphere shows the particle with the maximum value of flip-flops corresponding to the virial centre of the halo itself. The maximum number of flip-flops in the halo is 616 and the corresponding particle is very close to the centre of the virial sphere.

We conclude that it is feasible to expect that the flip-flop centres of DM haloes and subhaloes in Eulerian space can be reliably determined in cosmological *N*-body simulations by mapping the maxima of the flip-flop field found in Lagrangian space at least for sufficiently massive subhaloes.

7.2 Statistics of daughter peaks in the peak

First we look at the dependence of the number of daughter peaks defined as peaks within the parent peak. The parent peak is selected as a compact region at threshold $n_{\rm ff}^{\rm (peak,th)} = 100$. Then we continuously elevate the threshold $n_{\rm ff}^{\rm (daughter,th)} > n_{\rm ff}^{\rm (peak,th)}$ up to the highest maximum within the peak. We identify distinct daughter peaks with the number of particles greater than selected minimum at each level $n_{\rm ff}^{\rm (daughter,th)}$. We repeat this procedure for each of three minima: $N_{\rm p,min} = 100$, 50 and 25 particles. The bottom panel of Fig. 21 shows this dependence in the 256^3 simulation. Three lines show the effect of the minimal size of daughter peaks as indicated by the legend. For comparison and as an illustration of the effect of the simulation resolution, the top panel shows the substructure in the 128^3 simulation.[8] As expected the number of substructures increases with the resolution of the simulation and decreases with the growth of the size threshold $N_{\rm p,min}$. This is in a qualitative agreement with Figs 16 and 17.

[8] We are reminding that the common part of the Fourier amplitudes was the same in both simulations.

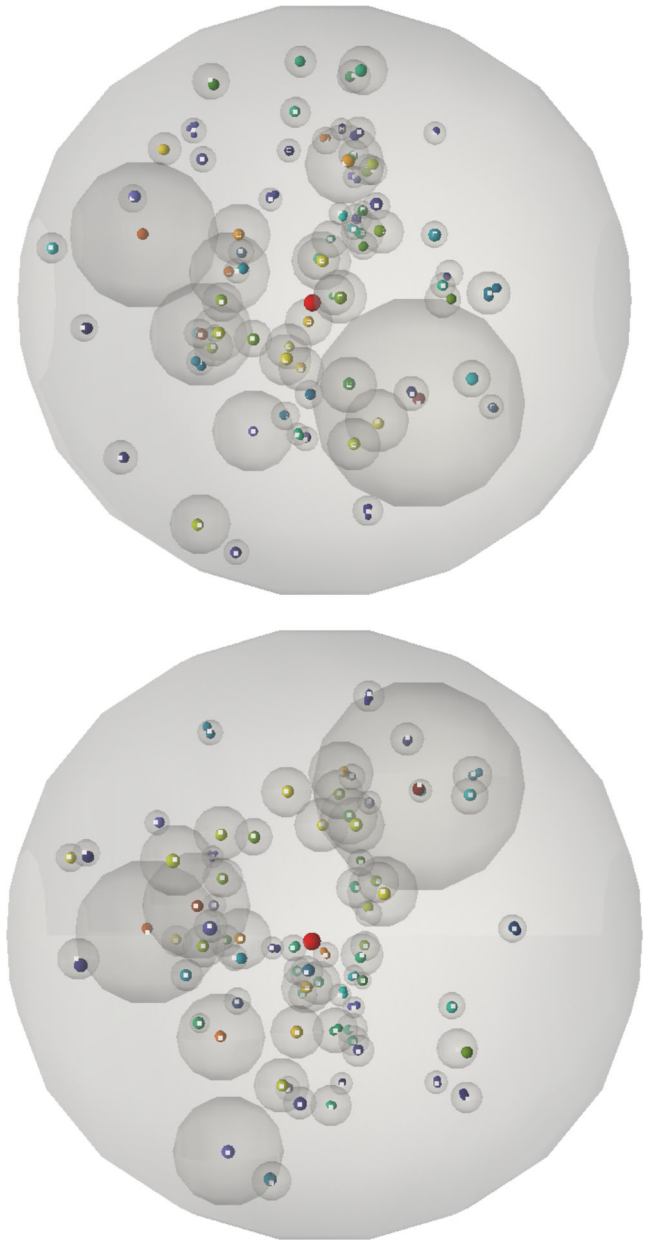

Figure 20. Two mutually orthogonal views of one of the largest halo along with its subhaloes in the simulation found by the AHF code. The haloes are represented by the spheres of the virial radii. Small coloured spheres mark the particles with the maximum value of the flip-flop field and white dots show the centres of the sphere, some of which may be obscured by the respective coloured spheres.

7.3 Selection of daughter peaks

In order to make an unambiguous case, we consider only substructures selected by two conditions: one by their masses or volumes in Lagrangian space that can be quantified by the number of particles $N_{\rm p,min} \geq 100$ and the other by their heights $n_{\rm ff}^{\rm (daughter,th)} \geq n_{\rm ff}^{\rm (peak,th)} = 100$. Therefore, we identify individual substructures within the parent peak at four thresholds: $n_{\rm ff} = 150, 240, 270$ and 300. The choice is based on the red curve in the bottom panel of Fig. 21.

The flip-flop daughter peaks in Lagrangian space are displayed as a set of marching cubes surfaces in Fig. 22. The parent peak in three-dimensional space represents a nesting structure resembling

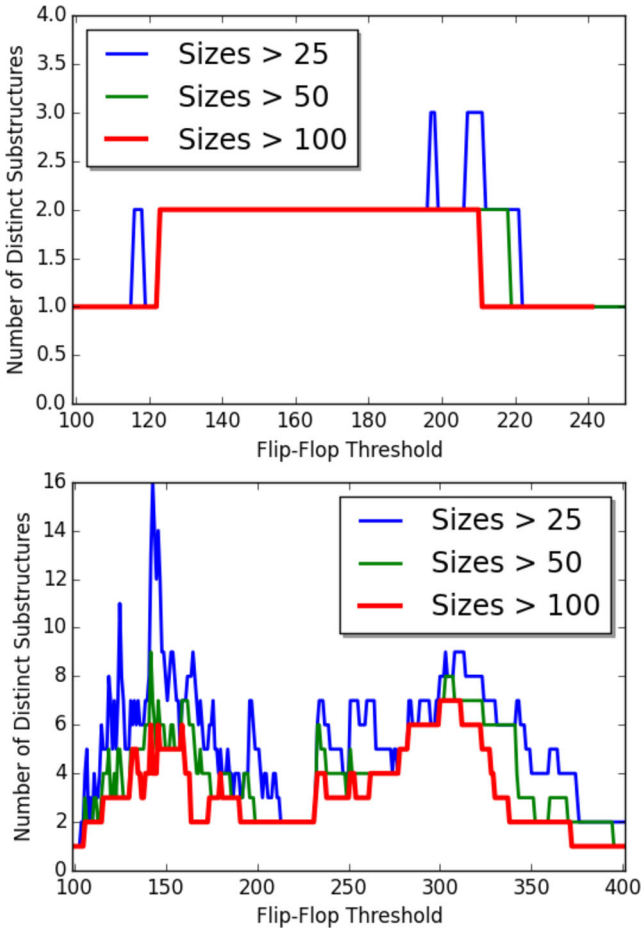

Figure 21. Number of daughter peaks within the largest flip-flop peak as a function of the threshold. The top and bottom panels correspond to the 128^3 and 256^3 simulations respectively. The lines of different colours show the dependence on the size threshold as indicated by the legend.

a generalized Russian doll or 'matreshka'-doll. Combining all five levels of this substructure in one plot significantly obscures the complex geometrical pattern of the peak. Therefore, we show the substructure in four steps each of which displays only two (top right) or three levels of the nesting structure: the lower level of substructure is shown as grey surfaces and the higher level as coloured surfaces, the light grey contour shows the parent peak. Colour scheme is same in every step: the colours (blue, magenta, cyan, green, yellow and red) correspond to the sizes/masses of daughter peaks in descending order. Thus the top left portion of Fig. 22 shows levels 100 and 150, top right – levels 100, 150 and 240, bottom left – levels 100, 240 and 270 and bottom right – levels 100, 270 and 300. The number of particles and masses of the peaks at every level are given in Tables 1 and 2.

It is worth stressing that Fig. 22 does not show the entire substructure of the halo shown in Fig. 20. Four thresholds were selected on the basis of the red line in the bottom panel of Fig. 21 as a few representative examples of substructure.

7.4 Illustration of the evolution of the flip-flop peak and seven daughter peaks selected at $n_{\rm ff} = 300$

In this section, we will closely follow the evolution of seven highest daughter peaks selected by the condition $n_{\rm ff} \geq 300$ and $n_{\rm part.} \geq 100$ at $z = 0$. We demonstrate that these daughter peaks become the nuclei

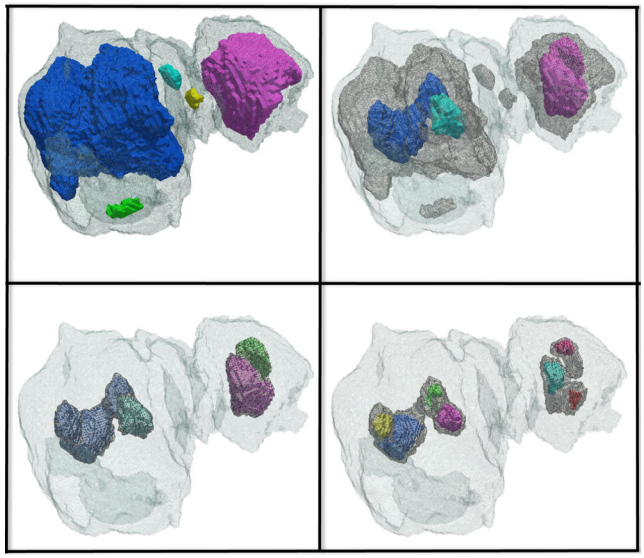

Figure 22. The marching cubes isosurfaces of the flip-flop field show five levels of hierarchical structure of the largest flip-flop peak in the 256^3 simulation in Lagrangian space. All panels show the surface of the peak identified as a connected region with $n_{\rm ff} \geq 100$ in light grey. The top right panel also shows five distinct daughter peaks at $n_{\rm ff} \geq 150$ in colour. The top right panel displays the surface at $n_{\rm ff} \geq 150$ in grey that are shown in the previous panel in colour. Three daughter peaks at $n_{\rm ff} \geq 240$ are shown in colour. The bottom subplots show three contours at $n_{\rm ff} = 240$ in grey and four at $n_{\rm ff} = 270$ in colour on the left and four contours at $n_{\rm ff} = 270$ in grey and seven at $n_{\rm ff} = 300$ in colour. Colours in order blue, magenta, cyan, green, yellow and red (two daughter peaks) correspond to the mass ranks of the daughter peaks from the largest to smallest one.

Table 1. Number of particles in substructures shown in Fig. 22.

Flip-flop threshold	N_1	N_2	N_3	N_4	N_5	N_6	N_7
100	206 670						
150	61 960	17035	513	308	265		
240	8698	3960	211				
270	4363	1474	753	521			
300	1976	416	405	381	286	267	178

Table 2. Approximate masses of substructures shown in Fig. 22 in units of $10^6\,{\rm M}_\odot$.

Flip-flop threshold	M_1	M_2	M_3	M_4	M_5	M_6	M_7
100	1464						
150	439	121	3.63	2.18	1.87		
240	61.6	28.1	1.50				
270	30.9	10.4	5.34	3.70			
300	14.0	2.94	2.87	2.70	2.03	1.89	1.26

of individual haloes and merge with each other in a hierarchical process of assembling the nucleus of the parent halo at early times $z > 24$ (Figs 23 and 24). Then we show how they evolve at $24 > z \geq 0$ after residing in the central region of the cloud formed by the particles of the parent peak (Fig. 25). It is worth stressing that only particles corresponding to the bottom right panel of Fig. 22 retain their colours in the plots described in this section. All the rest particles are black.

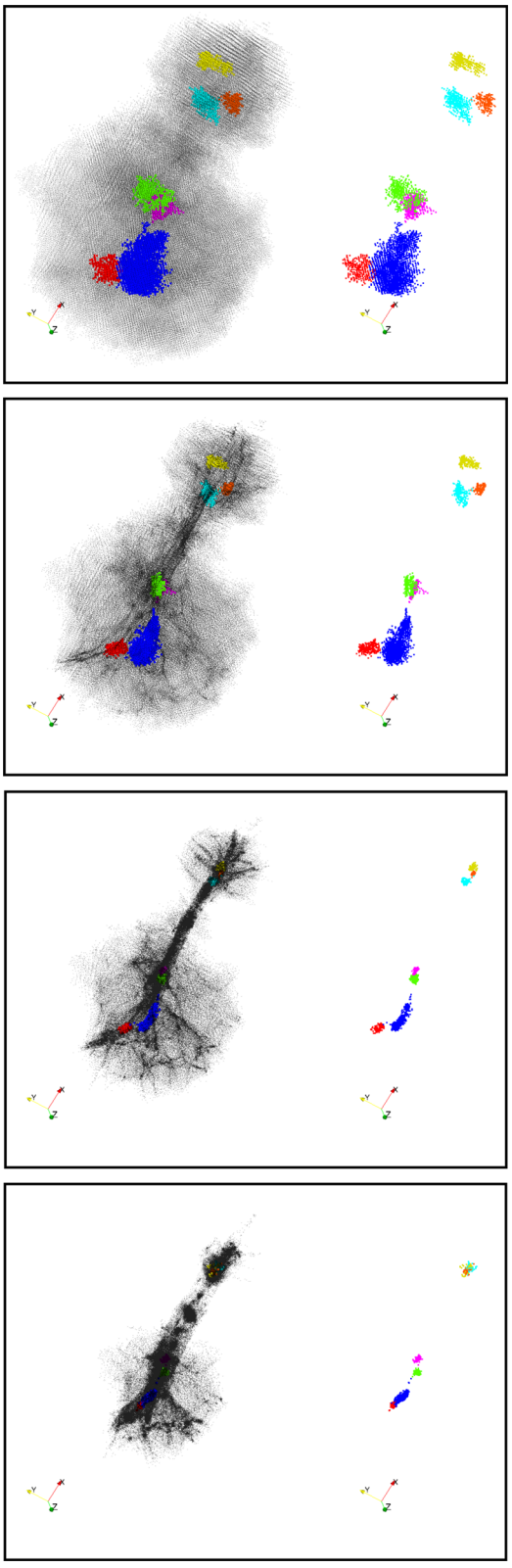

Figure 23. The figure illustrates the evolution of the particles in the parent peak selected at $n_{\rm ff} = 100$ level and coloured particles in seven daughter peaks selected at $n_{\rm ff} = 300$ level inside the parent peak. The plots on the left show all particles in the parent peak in grey and the particles of the daughter peaks are shown in colour on both sides. The stages from the top to bottom correspond to $z = 50, 42.6, 39.3, 36.2$ or respectively $a = 0.020, 0.023, 0.025, 0.027$. All plots have the same scale.

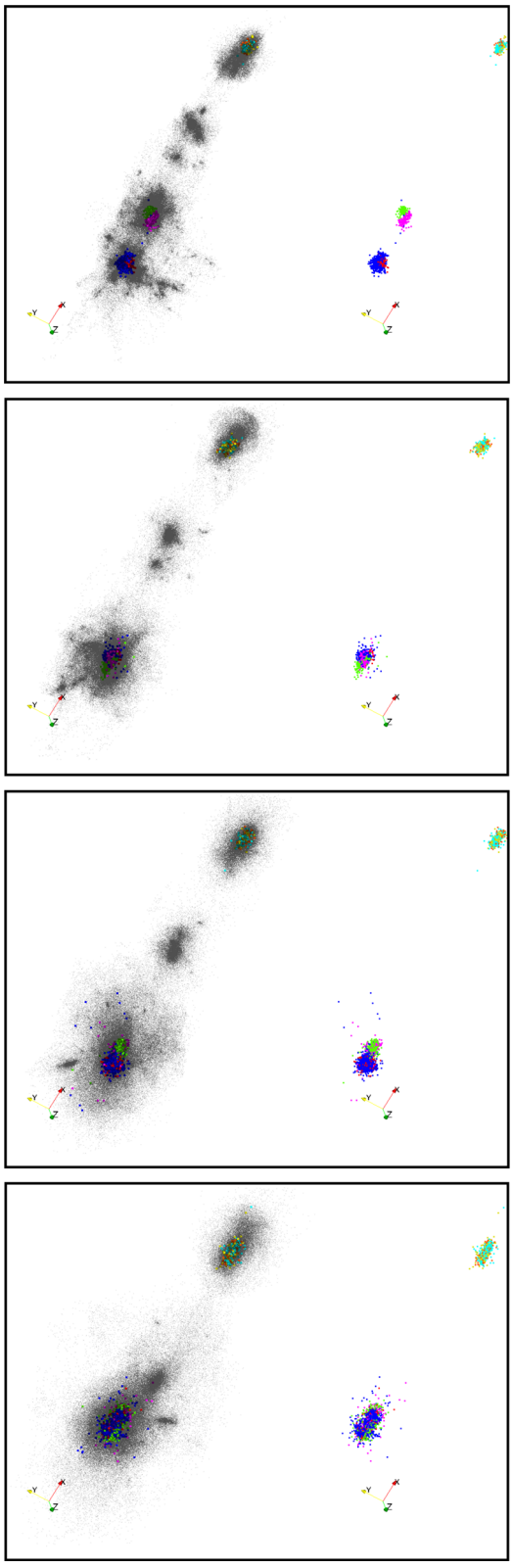

Figure 24. Same as Fig. 23 except the stages are $z = 33.4, 30.8, 28.4, 26.2$ or respectively $a = 0.029, 0.031, 0.034, 0.037$. In order to improve the visibility of subhaloes, the plots are progressively zoomed in with time.

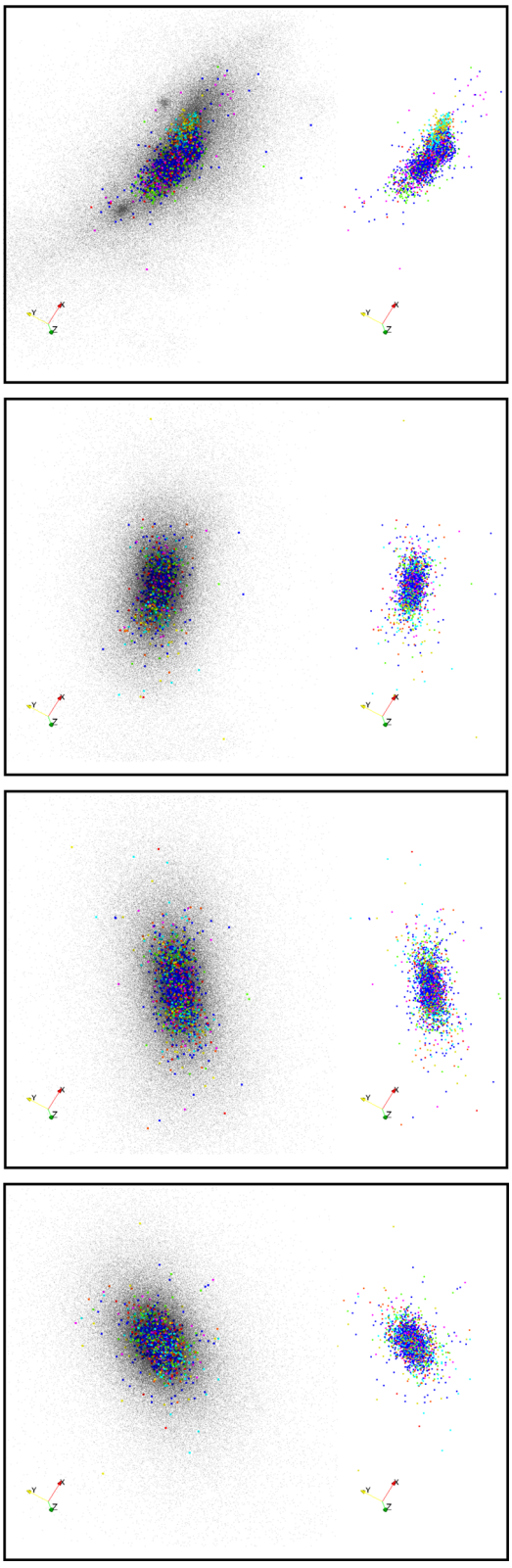

Figure 25. Same as Fig. 23 except the stages are $z = 24.1, 9.58, 3.82, 0$ or respectively $a = 0.040, 0.094, 0.21, 1.0$. In order to show subhaloes, the plots are arbitrary zoomed in.

As the bottom row of Table 1 shows, the total number of particles in seven highest peaks is 3909 which makes less than 2 per cent of 206 670 particles in the parent peak which in turn is a small nucleus of the halo with more than 16 million particles. Thus we consider a tiny fraction of the collapsed regions within a grey surface in the top left corner of Fig. 22, or black particles in the left part of top panel of Fig. 23.

We concentrate on this small set of particles because they reside in the highest density environment and thus have experienced the most vigorous dynamical evolution. The major issue we are interested in is the final state of particles in the selected seven daughter peaks of the flip-flop field. In particular is it feasible to identify them as distinct structures in Eulerian, velocity or phase spaces at $z = 0$?

Figs 23–25 show a sequence of dot plots illustrating the evolution of the selected particles in Eulerian space from $z = 50$ to $z = 0$ or respectively from $a = 0.02$ to $a = 1$. Each figure shows the structure formed by these particles at four redshifts indicated in the captions. It is no surprise that the colourful particles find themselves in the central parts of the cloud of black particles and thus become obscured very quickly. In order to show the structures formed by them more clearly, each of four panels in every figure is split into two parts: all particles are plotted on the left-hand side and only colourful particles are shown on the right-hand side. Please note that the orientation in Fig. 22 is similar but not identical to that in Figs 23–25. The orientations in Lagrangian and Eulerian spaces were chosen with the goal of minimizing obscuration due to projection.

The top panel in Fig. 23 shows Lagrangian space. The next panel shows the first output of the code at $z = 42.6$ when the flip-flop field on some particles becomes non-zero. By $z = 39.3$ shown in the third panel of Fig. 23, the colourful particles collapsed in small clumps embodied into a complicated filament formed by black particles.

The top panel of Fig. 24 shows that at $z = 33.4$ particles from seven peaks merged into three larger clumps approximately corresponding to the top right panel in Fig. 22. One can see four or even five haloes on the left-hand side of the top panel of Fig. 24 but only three of them contain colourful particles. The flip-flop peaks corresponding to two smaller haloes without colourful particles emerged from peaks lower than $n_{\rm ff} = 300$ level which was used for selecting the colourful particles. The rest panels of Fig. 24 illustrate the hierarchical process of merging of colourful particles. The bottom panel of Fig. 24 shows that all colourful particles merged into two compact clouds at the centres of two black clouds.

Fig. 25 displays the evolution after all colourful particles merged into a single cloud at $z = 24.1$ shown in the top panel. The remaining three panels show three states at $z = 9.58, 3.82$ and $z = 0$. The cloud of colourful particles is well mixed and remains intact after $z \approx 10$.

In order to see the central part of the halo, it has been zoomed in and the colourful particles are plotted with greater sizes than black particles. In addition, the opacity of black particles has been considerably reduced. Without this trickery, the colourful particles were hardly be visible at all in the panels on the left-hand side.

The outputs of the simulation are equally spaced in logarithm of the scalefactor a. Starting from the second from top panel in Fig. 23 until the top panel of Fig. 25 every output is displayed. Two middle panels of Fig. 25 show just two states in a long evolution from $z = 24.1$ shown at the top to $z = 0$ shown at the bottom. There are probably two remarkable features in this evolution. First, the orientation of both the central part of the halo depicted by the colourful particles and 50 times more massive part of the halo shown by black particles substantially and synchronously have changed their orientation. This obviously happened because they are only small central parts of a much more massive halo experienced

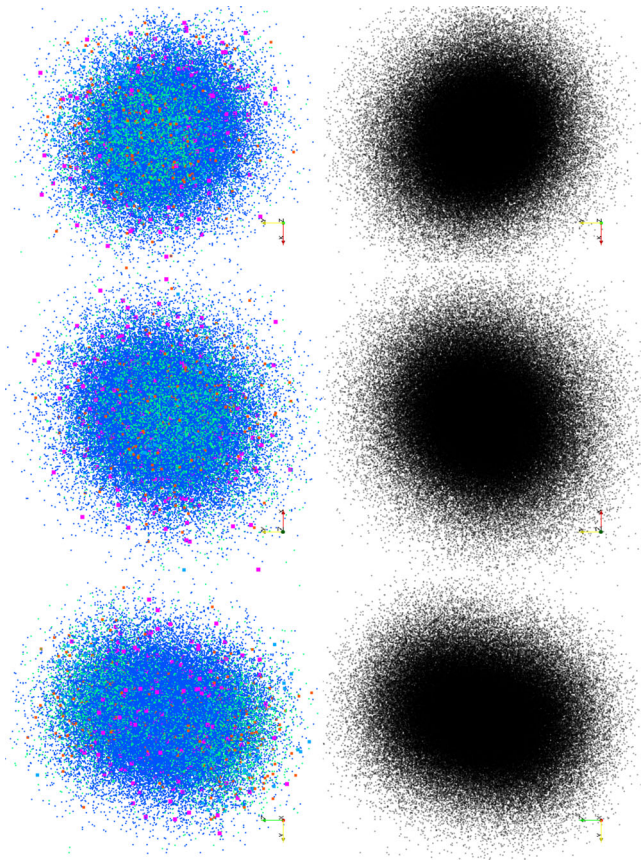

Figure 26. Velocity space. Three mutually orthogonal projections of the particles from the peak of the flip-flop field discussed in the previous section is shown in black. Five daughter peaks selected at $n_{\rm ff} = 150$ level (see Tables 1 and 2) shown in colour on the left. The orientations and sizes of the clouds on the left-hand and right-hand sides are synchronized in each projection. The colours of particles are similar to those in Figs 22–25. In order to make the particles in small daughter peaks visible, the sizes of dots are increasing with decreasing of the number of particles in the daughter peak.

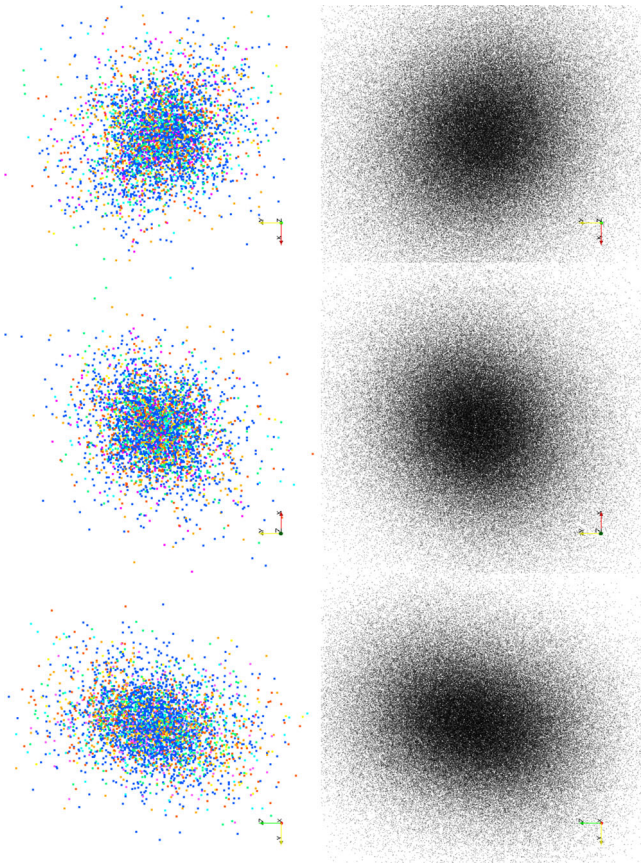

Figure 27. Same as Fig. 26 except the particles of seven daughter peaks selected at $n_{\rm ff} = 300$ level (see Tables 1 and 2). Note that the scale is smaller than that in Fig. 26 and the opacity in the right column is reduced by 60 per cent.

considerable accretion of mass. Secondly, the final state shown by coloured particles looks like a dynamically relaxed configuration with all seven daughter peaks marked by different colours well mixed. Nevertheless they are easily identified as distinct peaks of the flip-flop field in Lagrangian space $n_{\rm ff}(\boldsymbol{q}, z = 0)$ in Fig. 22. Next we show the distribution of coloured and black particles in the velocity and two-dimensional projection of phase space.

7.5 The flip-flop peak in velocity space at $z = 0$

Three mutually orthogonal projections of the velocity space at $z = 0$ is shown in Figs 26 and 27. The particles in the parent peak with number of flip-flops greater than 100 are shown in black on the right of both figures. Coloured particles shown on the left are from five daughter peaks selected above 150 flip-flops in Fig. 26 and from seven daughter peaks selected above 300 flip-flops in Fig. 27. If coloured particles from the daughter peaks were plotted together with the particles of the parent peak, they would be completely obscured by the particles in the parent peak.

The colours of the particles in Figs 26 and 27 correspond to the colours in the top left and bottom right panels of Fig. 22 respectively. In order to see the particles of three smallest daughter peaks in Fig. 27, the sizes of the particles were substantially increased. In addition, the opacity in the right-hand panels were reduced by 40 per cent.

Similarly to the impression from spatial distributions of particles shown in bottom panels of Fig. 25, the particles of the daughter peaks look also well mixed in velocity space. The velocity distributions look slightly ellipsoidal as they should because the spatial distributions are also slightly ellipsoidal. Nevertheless the peaks of the flip-flop field are easily distinguishable in Lagrangian space as Figs 4, 6 and 22 demonstrate. Finally, we consider the distributions of the particles in the parent and daughter peaks in two-dimensional projection of six-dimensional phase space in the next section.

7.6 Phase space

In order to illustrate the structure of the halo, we plot the distribution of particle in two-dimensional 'phase space': the radial component of the velocities versus radii of the particles in Figs 28 and 29 corresponding to $z = 24.1$ and $z = 0$, respectively. The mean coordinates and velocities of all particles in the parent peak serve as the origin in phase space. Colours show the number of flip-flops experienced by each particle.

Fig. 28 show a major merger of two subhaloes. By the present time $z = 0$ shown in Fig. 29, all traces of the merger seem to disappear. The distribution of the particles in the phase space looks quite regular and structureless.

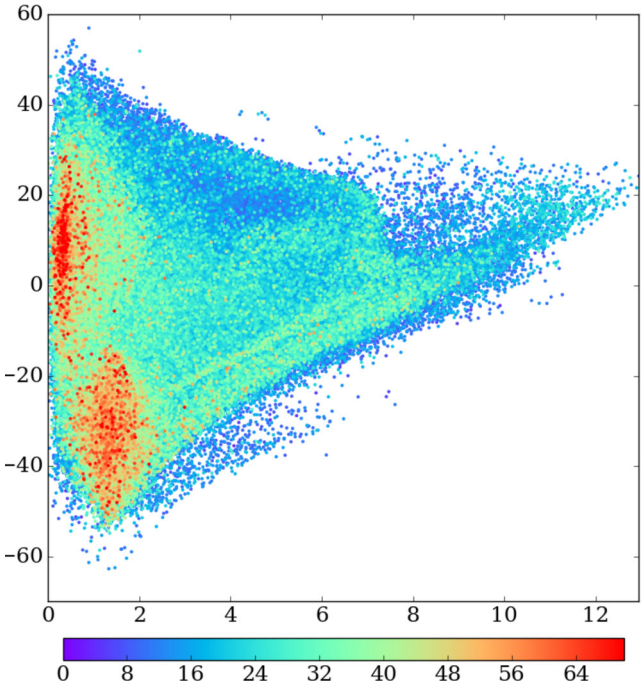

Figure 28. Phase-space structure of the particles in the parent peak at $z = 24.1$. At this stage, as also shown in configuration space in the top panel of Fig. 25, the coloured particles experience the last major merger. The colours of the particles show the number of flip-flops as indicated by the colour bar. The distances and velocities are given in comoving kpc and km s^{-1} respectively.

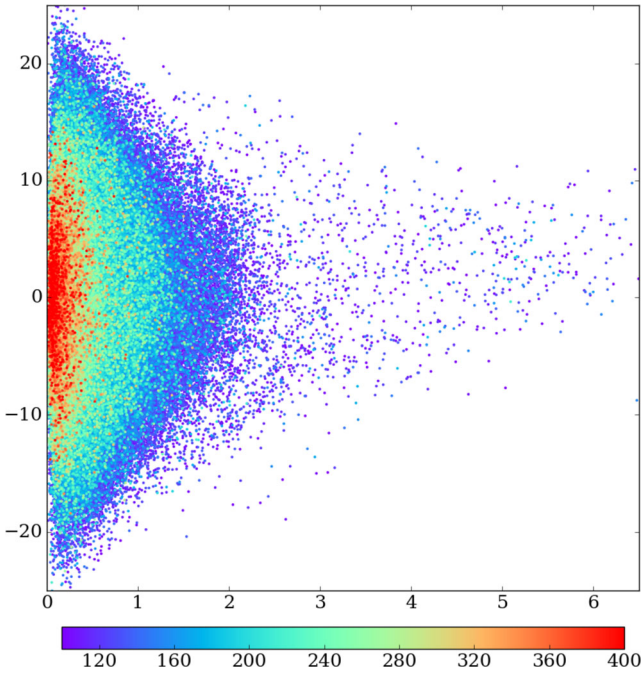

Figure 29. Phase-space structure of the peak shown in the bottom panel of Fig. 25 at $z = 0$. Colour bar is marked by the number of flip-flops of the particles.

Finally, Fig. 30 shows the particles in four sets of the daughter peaks selected at four thresholds $n_{\rm ff} \geq 150$, 240, 270, 300 of the flip-flop field in Lagrangian space at $z = 0$. The daughter peaks corresponding to four different thresholds are shown separately in four panels arranged in ascending order of the thresholds from top left to top right then to bottom left and then to bottom right. The particles are plotted in the same order thus the peaks with fewer particles are plotted on the top of larger peaks. The phase portraits of the daughter peaks seem to agree with the distributions in configuration and velocity spaces: the eyes see no particular structures if colours are removed.

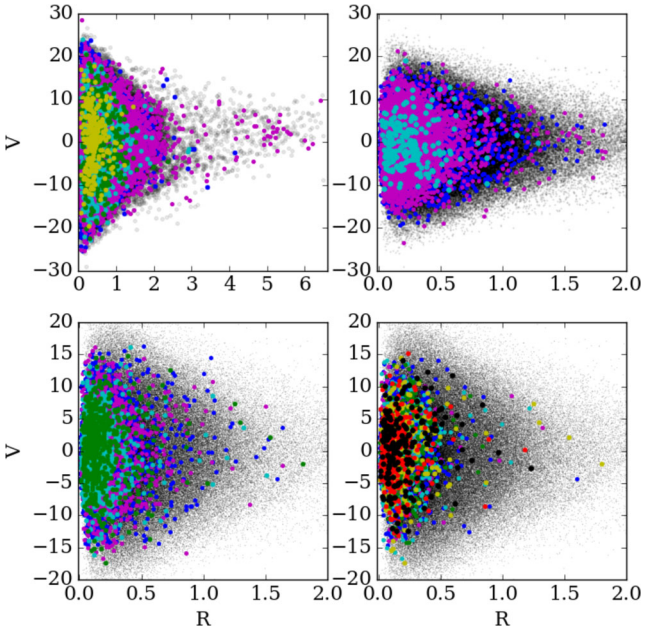

Figure 30. Phase-space structure of the parent (black dots) and daughter peaks selected at four levels $n_{\rm ff} = 150$, 240, 270, 300 (coloured dots) in four panels from top left to top right to bottom left and to bottom right bottom right respectively is shown at $z = 0$. As before the colours are blue, magenta, cyan, green, yellow, red and black mark the rank of the peak in the decreasing order of the number of particles, see Tables 1 and 2. The distances and velocities are given in kpc and km s^{-1} respectively.

8 SUMMARY

Although the phenomenon of flip-flopping has been known for a long time and used in cosmological *N*-body simulations notably by Vogelsberger & White (2011) and Falck et al. (2012), our work represents the first attempt of systematic study of flip-flopping phenomenon as a field in Lagrangian space.

We explored the properties of the flip-flop field in the *N*-body simulations designed to simulate the formation of DM haloes at early stage of the evolution of the universe $z > 35$ (see Fig. 23). These small haloes were identified as the peaks of the flip-flop field computed at $z = 0$ (see Figs 21 and 22). We followed seven highest daughter peaks in the flip-flop field $n_{\rm ff}(\boldsymbol{q}, z = 0)$ within the largest peak in the simulation with 256^3 particles.

We demonstrated that the selected seven peaks were initially individual small haloes (Fig. 23). Then they experienced multiple mergers (Fig. 24) and finally merged in a single approximately ellipsoidal cloud at the centre of the parent halo (two top panels of Fig. 25). During the following evolution from at least $z \sim 10$ or even earlier the merged seven peaks remained in the central region of the halo. Although the orientation of the ellipsoid significantly changed but it remained intact until $z = 0$ as Fig. 25 demonstrates. It is remarkable that despite a very vigorous mixing in Eulerian configuration space the flip-flop field retains a 'record' of the merging

history in the form of easily identified isolated peaks (see Figs 21 and 22).

The distributions of the particles from these peaks in velocity space (Figs 26 and 27) look as well-mixed clouds with slightly ellipsoidal shapes. Moreover the two-dimensional projections of the six-dimensional phase space also show no traces of substructure in the distribution of these particles at $z = 0$ (Fig. 29) while at $z = 24.1$ two subhaloes are clearly seen in Fig. 28. The distributions of particles in all daughter peaks selected at four levels $n_{\rm ff} = 150$, 240, 270, 300 shown separately in four panels of Fig. 22 also provide no signs of substructure as Fig. 30 demonstrates. In our simulations, the force resolution exceeded the mass resolution by 5.2 times thus we cannot exclude that the absence of a clear signature of substructure in configuration, velocity and phase spaces is related to violation of the requirement of the simulation to be collisionless (see e.g. Melott et al. 1997; Hahn et al. 2013). This requires special simulations and analysis that is left for further paper.

In order to gain a clue to understanding whether this property is unique to the flip-flop field or in some form is also present in other fields, we made a statistical comparison with density and potential fields generated *on particles*. We used a number of different statistics in order to quantify the differences between flip-flop, density and potential fields. For instance the cumulative probability function of the flip-flop field demonstrates an obvious monotonic evolution with time while that of density field shows a considerably less clear signal (see Figs 7 and 8). We also estimated the correlation coefficients between the same field at two different stages (Fig. 12). The last statistics provides a strong evidence of a remarkable stability of the geometry of the flip-flop field over time. This conclusion is also strongly supported by the statistics of the ratio of the field taken at a reference epoch to the field taken at each preceding epoch. Fig. 13 clearly demonstrates that the geometry of the flip-flop field is incomparably more stable than the potential or density field computed *on particles*.

We conclude that the unprecedented stability of the flip-flop field in Lagrangian space can be explained by a simple assumption. The fluid elements of gravitating collisionless medium experienced first flip-flopping earlier than others tend to keep the time between following flip-flops shorter. Thus they retain positions among the leaders in the flip-flop counts as demonstrated by two statistics displayed in Figs 14 and 15. The time between sequential flip-flops of a fluid element is a characteristic time between its most significant dynamical metamorphoses. The dynamical significance of each flip-flop may be attributed to passing of the fluid element through the state of infinite density. Thus counting the flip-flops of a fluid element can be considered as counting ticks of its own dynamical clock. We demonstrated that there is a sort of dynamical instability: the greater the current counts of flip-flops the more probable the next (see Fig. 14). This results in the remarkable stability of the geometry of the flip-flop field, because the particles with lower counts of flip-flops have little chance to overtake their neighbours with currently higher flip-flop counts. In other words, it is very unlikely that the valleys of the flip-flop field will become peaks (see Fig. 2).

Still the further confirmation of the previous conclusions comes from the time evolution of the number of peaks as a function of the filling factor. It is displayed in Figs 16 and 17 for 128^3 and 256^3 simulations respectively.

The final flip-flop field looks like a set of bulky regions well isolated by narrow valleys, see Figs 1, 2 and 4 for one-, two- and three-dimensional examples respectively. The peaks in Lagrangian space typically have a highly nested structure consisting of several smaller by sizes daughter peaks which in turn may consist of even smaller peaks. The hierarchy can be wide-ranging in sizes of peaks and therefore in their masses. The geometry of the flip-flop field seems to be very different from a Gaussian field as a visual inspection suggests (see Figs 4 and 6).

The geometry of the flip-flop landscape evolves rapidly after the onset of strong non-linearity marked by emerging of the first regions with $n_{\rm ff}(\boldsymbol{q}, z_{\rm nl}) > 0$. Then its evolution is considerably impeded (see Figs 12 and 13) almost to complete freeze while the heights of peaks continue to grow. The latter indicates ongoing rapid dynamics inside the haloes and subhaloes themselves while the former suggests a remarkable stability of the flip-flop landscape in Lagrangian space.

We are suggesting the following explanation why only the flip-flop field has these unique characteristics. The flip-flop field represents a very complicated structure of dark matter haloes and subhaloes in six-dimensional phase space in the form of a much simpler set of tree-like structures in only four dimensions made by three Lagrangian axes and the number of flip-flops axis. Thus, the simplification is not only due to reduction of the number of dimensions but more importantly by the fact that the flip-flop distribution in Lagrangian space is a single-valued function i.e. a three-dimensional field.

We conclude that the flip-flop field $n_{\rm ff}(\boldsymbol{q}, z)$ carries a wealth of information about substructures in the collisionless Cosmic Web. In particular, the peaks of the flip-flop field at the final stage $n_{\rm ff}(\boldsymbol{q}, z = 0)$ store substantial information about the history of mergers. The described properties of the flip-flop field and easiness of its computing in cosmological *N*-body simulations make it a good candidate for a valuable addition to the suite of various techniques suggested for studies of substructures in the dark matter Cosmic Web and its evolution.

ACKNOWLEDGEMENTS

SS acknowledges support by the Templeton Foundation program 'The emergence of complex structural patterns: A manifistation of increasing cosmic complexity' and sabbatical support at Kapteyn Astronomical Institute at the University of Groningen The Netherlands and by Argonne National Labs where the significant part of the work was done. SS also thanks S. Habib for fruitful discussions. The authors are grateful to S.D.M. White for useful critical comments on the first draft of the paper. MM acknowledges partial support by DOE and NSF via grants DE-FG02-07ER54940 and AST-1209665. The authors are grateful to the anonymous referee for useful suggestions and constructive criticism.

REFERENCES

Abel T., Hahn O., Kaehler R., 2012, MNRAS, 427, 61
Arnold V. I., Shandarin S. F., Zeldovich Y. B., 1982, Geophys. Astrophys. Fluid Dyn., 20, 111
Ascasibar Y., Binney J., 2005, MNRAS, 356, 872
Benson A. J., 2012, New Astron., 17, 175
Cautun M., van de Weygaert R., Jones B. J. T., Frenk C. S., 2014, MNRAS, 441, 2923
Colberg J. M. et al., 2008, MNRAS, 387, 933
Couchman H. M. P., Carlberg R. G., 1992, ApJ, 389, 453
Davis M., Efstathiou G., Frenk C. S., White S. D. M., 1985, ApJ, 292, 371
Diemand J., Moore B., Stadel J., 2005, Nature, 433, 389
Falck B. L., Neyrinck M. C., Szalay A. S., 2012, ApJ, 754, 126
Ghigna S., Moore B., Governato F., Lake G., Quinn T., Stadel J., 1998, MNRAS, 300, 146
Gill S. P. D., Knebe A., Gibson B. K., 2004, MNRAS, 351, 399

Gurbatov S. N., Saichev A. I., Shandarin S. F., 1985, Sov. Phys. Dokl., 30, 921
Gurbatov S. N., Saichev A. I., Shandarin S. F., 1989, MNRAS, 236, 385
Gurbatov S. N., Saichev A. I., Shandarin S. F., 2012, Phys. Usp., 55, 223
Hahn O., Angulo R. E., 2016, MNRAS, 455, 1115
Hahn O., Abel T., Kaehler R., 2013, MNRAS, 434, 1171
Hidding J., van de Weygaert R., Vegter G., Jones B. J. T., Teillaud M., 2012a, MNRAS, preprint (arXiv:1205.1669)
Hidding J., van de Weygaert R., Vegter G., Jones B. J. T., 2012b, preprint (arXiv:1211.5385)
Hoffmann K. et al., 2014, MNRAS, 442, 1197
Klypin A., Gottlöber S., Kravtsov A. V., Khokhlov A. M., 1999, ApJ, 516, 530
Knebe A. et al., 2013, MNRAS, 435, 1618
Knollmann S. R., Knebe A., 2009, ApJS, 182, 608
Kofman L., Pogosyan D., Shandarin S. F., Melott A. L., 1992, ApJ, 393, 437
Landau L. D., Lifshitz E. M., 2008, Mechanics. Course of Theoretical Physics, Vol. 1. Elsevier, Amsterdam
Melott A. L., Shandarin S. F., Splinter R. J., Suto Y., 1997, ApJ, 479, L79
More S., Diemer B., Kravtsov A. V., 2015, ApJ, 810, 36
Neyrinck M. C., 2012, MNRAS, 427, 494
Neyrinck M. C., Falck B. L., Szalay A. S., 2015, in Rosquist K., ed., Thirteenth Marcel Grossmann Meeting: On Recent Developments in Theoretical and Experimental General Relativity, Astrophysics and Relativistic Field Theories. World Scientific Publ., p. 2136
Okamoto T., Habe A., 1999, ApJ, 516, 591
Powell D., Abel T., 2015, J. Comput. Phys., 297, 340
Ramachandra N. S., Shandarin S. F., 2015, MNRAS, 452, 1643
Ramachandra N. S., Shandarin S. F., 2017, MNRAS, 467, 1748
Shandarin S. F., 1983, Sov. Astron. Lett., 9, 104
Shandarin S. F., Medvedev M. V., 2014, preprint (arXiv:1409.7634)
Shandarin S. F., Medvedev M. V., 2016, in van de Weygaert R., Shandarin S., Saar E., Einasto J., eds, Proc. IAU Symp. 308, The Zeldovich Universe: Genesis and Growth of the Cosmic Web. Cambridge Univ. Press, Cambridge, p. 103
Shandarin S., Zeldovich Y., 1989, Rev. Mod. Phys., 61, 185
Shandarin S., Habib S., Heitmann K., 2012, Phys. Rev. D, 85, 083005
Sousbie T., Colombi S., 2016, J. Comput. Phys., 321, 644
Springel V., 2005, MNRAS, 364, 1105
Suginohara T., Suto Y., 1992, ApJ, 396, 395
Summers F. J., Davis M., Evrard A. E., 1995, ApJ, 454, 1
van Kampen E., 1995, MNRAS, 273, 295
Vogelsberger M., White S. D. M., 2011, MNRAS, 413, 1419
Zel'dovich Y. B., 1970, A&A, 5, 84
Zeldovich Y. B., Einasto J., Shandarin S. F., 1982, Nature, 300, 407

This paper has been typeset from a TEX/LATEX file prepared by the author.